



# FESOM2.1-REcoM3-MEDUSA2: an ocean–sea ice–biogeochemistry model coupled to a sediment model

Ying Ye<sup>1</sup>, Guy Munhoven<sup>2</sup>, Peter Köhler<sup>1</sup>, Martin Butzin<sup>1,3</sup>, Judith Hauck<sup>1,4</sup>, Özgür Gürses<sup>1</sup>, and Christoph Völker<sup>1</sup>

<sup>1</sup>Alfred-Wegener-Institut Helmholtz-Zentrum für Polar- und Meeresforschung, P.O. Box 12 01 61, 27515 Bremerhaven, Germany

<sup>2</sup>Laboratoire de Physique Atmosphérique et Planétaire, Université de Liège, 4000 Liège, Belgium

<sup>3</sup>MARUM – Center for Marine Environmental Sciences, University of Bremen, Bremen, Germany

<sup>4</sup>Faculty of Biology/Chemistry, University of Bremen, Bremen, Germany

**Correspondence:** Ying Ye (ying.ye@awi.de)

Received: 4 September 2023 – Discussion started: 6 September 2023

Revised: 31 August 2024 – Accepted: 19 December 2024 – Published: 21 February 2025

**Abstract.** This study describes the coupling of the process-based Model of Early Diagenesis in the Upper Sediment with Adaptable complexity (MEDUSA version 2) to an existing ocean biogeochemistry model consisting of the Finite-volume Sea ice–Ocean Model (FESOM version 2.1) and the Regulated Ecosystem Model (REcoM version 3). Atmospheric CO<sub>2</sub> in the model is a prognostic variable which is determined by the carbonate chemistry in the surface ocean. The model setup and its application to a pre-industrial control climate state is described in detail. In the coupled model, 1390 PgC is stored in the top 10 cm of the bioturbated sediment, mainly as calcite, but also as organic matter (10%). In the coupled simulation, atmospheric CO<sub>2</sub> stabilizes at ~ 295 ppm after 2000 years, in line with the CO<sub>2</sub> level expected from the climate forcing conditions. Sediment burial of carbon, alkalinity, and nutrients in the coupled simulation is set to be compensated by riverine input. The spatial distribution of biological production is altered depending on the location of riverine input and reduction in sedimentary input, as well as the strength of local nutrient limitation, while the global productivity is not affected substantially. With this coupled ocean–sediment system the model is able to simulate the carbonate compensation feedback under moderate perturbation of CO<sub>2</sub> in the atmosphere.

## 1 Introduction

The ocean plays a key role in the global carbon cycle. It stores about 37 200 PgC (Keppler et al., 2020), more than 40 times as much carbon as the atmosphere, which contained 884 PgC (or 417 ppm) in the year 2022 (Lan et al., 2023). About 25 %–30 % of the global anthropogenic CO<sub>2</sub> emissions are taken up by the world oceans (Friedlingstein et al., 2022).

CO<sub>2</sub> enters the ocean through gas exchange, where it dissolves in seawater. A unique feature of dissolved CO<sub>2</sub> is that it reacts with water to form carbonic acid (H<sub>2</sub>CO<sub>3</sub>), which is instable and dissociates as a function of temperature, salinity, and pressure into bicarbonate (HCO<sub>3</sub><sup>-</sup>), carbonate (CO<sub>3</sub><sup>2-</sup>), and hydrogen (H<sup>+</sup>) ions (Zeebe and Wolf-Gladrow, 2001). The dissolved inorganic carbon (DIC), which is the sum of CO<sub>2</sub>, HCO<sub>3</sub><sup>-</sup>, and CO<sub>3</sub><sup>2-</sup>, is distributed in the ocean via circulation. Part of the carbon in the surface ocean is also taken up via photosynthesis by marine phytoplankton and exported into the ocean interior via the sinking of dead organic matter. When stored in the deep ocean, this carbon reduces the surface concentration of DIC and allows further CO<sub>2</sub> uptake from the atmosphere. Another important process in the marine carbon cycle is driven by calcifying plankton. These organisms produce calcium carbonate (CaCO<sub>3</sub>) shells whereby CO<sub>2</sub> is released back into the atmosphere. These processes, which all influence the surface-to-depth-gradient in DIC, are also summarized as the so-called marine carbon pumps (Volk and Hoffert, 1985). Some of the particulate carbon (i.e. par-

ticulate organic carbon (POC) and  $\text{CaCO}_3$ , ca. 1 % of primary production; Sarmiento and Gruber, 2006) escapes dissolution and remineralization in the water column and sinks to the seafloor, where it might be buried. These particles are then removed from the relatively fast cycling of carbon at the surface of the Earth.

The storage of carbon, alkalinity, and nutrients in sediments introduces an additional slow timescale to carbon cycling and increases the carbon storage in the sediment–ocean system overall. The global burial flux of particulate organic carbon in marine sediments has been reported to be in a range of 160–2600  $\text{PgC kyr}^{-1}$  (Burdige, 2007; Dunne et al., 2007; Sarmiento and Gruber, 2006; Muller-Karger et al., 2005). In total,  $\sim 280 \text{PgC kyr}^{-1}$  is buried as  $\text{CaCO}_3$  in marine sediments, of which 100–150  $\text{PgC kyr}^{-1}$  find their way into sediments of the deep sea (below at least 1 km of water depth) (Sarmiento and Gruber, 2006; Dunne et al., 2012; Cartapanis et al., 2018; Hayes et al., 2021). Furthermore, marine sediments play an important role, as they provide records of the Earth's past climate. They react via the carbonate compensation feedback to any changes in the marine carbon cycle, in which the deep-ocean carbonate ion concentration is brought back to its initial values after a perturbation on a multi-millennial timescale via sediment dissolution of  $\text{CaCO}_3$  (Broecker and Peng, 1987).

Anthropogenic carbon emissions represent a rapid carbon cycle perturbation and, in high-emission scenarios (Meinshausen et al., 2011), may ultimately lead to the massive dissolution of  $\text{CaCO}_3$  in seafloor sediments over the next millennia (Archer et al., 1997). This carbonate compensation feedback contributes to a reduction in the long-term airborne fraction of anthropogenically emitted  $\text{CO}_2$  from more than 20 % if only the atmosphere–ocean is considered to be less than 10 % (Archer et al., 2009; Köhler, 2020). This additional oceanic uptake of anthropogenic carbon through the dissolution of  $\text{CaCO}_3$ , however, operates on a multi-millennial timescale and is therefore only of interest for the geological fate of fossil emissions but not for our near future. Hence, understanding processes controlling the sediment–ocean exchange and quantifying the carbon storage in marine sediments is crucial to explain transient behaviour over changing climates, e.g. the glacial–interglacial  $\text{CO}_2$  variations (e.g. Brovkin et al., 2012; Köhler and Munhoven, 2020), and to predict the long-term ocean sequestration of anthropogenic carbon (Archer et al., 2009; Köhler, 2020).

All ocean biogeochemistry models incorporate a scheme to describe the fate of biogenic material that reaches the seafloor but differ in their complexity (Munhoven, 2021, and references therein). The most simple schemes start from a reflective boundary condition, where all material reaching the seafloor is remineralized and returned to solution. More complex schemes consider a single, vertically integrated mixed-layer sediment box with complete mass balances for the particles settling to the seafloor. Even higher complexity is found in vertically resolved sediment models describing dia-

genetic reactions, mechanical changes in dissolved and solid components, and burial fluxes out of the surface sediment.

FESOM2.1-REcoM3, consisting of the Finite-volume Sea Ice–Ocean Model 2.1 and the Regulated Ecosystem Model 3, is one of the ocean biogeochemistry models, which so far includes a simple one-layer sediment model (Gürses et al., 2023). REcoM3 describes the marine ecosystem at medium complexity with two phytoplankton classes, including silicifiers and calcifiers, and two zooplankton classes, representing mixed zooplankton and polar macrozooplankton, and it considers flexible stoichiometry of C, N, Si, Fe,  $\text{CaCO}_3$ , and chlorophyll. Two external iron sources (sediment and dust) are implemented into REcoM3, and the model also has the option to simulate the cycles of  $^{13}\text{C}$  and  $^{14}\text{C}$  (Butzin et al., 2024). The sediment box used so far in REcoM3 ensures the mass conservation by a complete remineralization of material sinking into the box. It represents processes in the surface sediment and is useful for short-term simulations, since the characteristic timescales of early diagenetic processes are often of the order of days to months, while long-term burial via sedimentation (which compensates riverine inputs from continental weathering) acts on timescales of thousands of years. Kriest and Oschlies (2013) showed that the introduction of a sediment box makes models more robust against the uncertainties of the remineralization length scale compared to models that remineralize everything in the water column. However, without considering sediment–ocean fluxes and feedbacks in more detail, the model would not be able to reasonably simulate transient changes over glacial/interglacial timescales.

In Sect. 2, we describe the coupling of FESOM2.1-REcoM3p, a model configuration targeted for palaeo-application, with MEDUSA2, the Model of Early Diagenesis in the Upper Sediment with Adaptable complexity (Munhoven, 2021). MEDUSA2 is a process-based sediment module that offers a complex alternative to the previously used simple one-layer sediment. This is the first realization of such an ocean–sediment setup of the marine carbon cycle with flexible stoichiometry of organic matter. In comparable existing alternatives (e.g. Kurahashi-Nakamura et al., 2020; Moreira Martinez et al., 2016), stoichiometry was kept fixed. This feature enables our model to simulate the growth limitation and community composition of phytoplankton in a more realistic way so that the biological carbon pump has a higher flexibility to react to climate change (Seifert et al., 2022; Schartau et al., 2007; Hohn, 2009). The final model configuration, referred to as FESOM2.1-REcoM3p-MEDUSA2, is applicable to relevant questions in palaeoclimate research and should be able to provide new insights into the long-term dynamics of the marine carbon cycle. The coupled ocean–sediment simulation of this configuration under pre-industrial climate conditions is analysed in Sect. 3, along with transient simulations with perturbations in atmospheric  $\text{CO}_2$ , while its applications to questions of the last glacial cycle are envisaged in future, more targeted studies.

## 2 Methods

### 2.1 Model description

#### 2.1.1 REcoM3p: a REcoM3 configuration for palaeo-research

REcoM is an ocean biogeochemistry and ecosystem model describing cycles of carbon, oxygen, and nutrients (nitrogen, silicon, and iron) with varying intracellular stoichiometry in phytoplankton, zooplankton, and detritus. REcoM3 is the most recent release version, and a detailed description of this version, including its coupling to FESOM2.1, is given by Gürses et al. (2023). The configuration REcoM3p used here has reduced complexity with respect to functional groups of the modelled ecosystem and considered only one generic zooplankton and one detritus class, instead of two in the full version of REcoM3 (Fig. 1). As in the full version, diatoms and small phytoplankton which include calcifiers (only calcite producers, no aragonite) are considered here. The total 22 biogeochemical tracers cover nutrients (DIN – dissolved inorganic nitrogen; DSi – dissolved silicon; DFe – dissolved iron); two types of phytoplankton (diatoms and small phytoplankton) with the state variables C, N, and chlorophyll and biogenic silica in diatoms and calcite in small phytoplankton; one zooplankton with C and N pools; one detritus with the state variables C, N, calcite, and opal; dissolved organic matter with C and N pools; DIC; alkalinity (Alk); and oxygen. The biological cycling of iron is described using a fixed Fe : N ratio in phytoplankton, zooplankton and detritus. The same parameter values were used as described in Gürses et al. (2023), and only two parameters were tuned for the reduced food web and coarser resolution (see Table B1 in the Appendix).

So far, REcoM3 only included a single-layer sediment. Particles sinking out of the bottom water boxes enter this sediment layer and go through remineralization (of organic particles) and dissolution (of calcite and opal) following a simple first-order decay approach: organic matter remineralization is neither dependent on O<sub>2</sub> availability nor follows different redox pathways; carbonate dissolution proceeds irrespective of the ambient saturation state (similarly to the dissolution in the water column). The approach is thus equivalent to a classical reflective boundary with temporal buffering. The fluxes of solutes back to the bottom water boxes are derived from the remineralization and dissolution rates of the solids via the elemental ratios that characterize them. While the main aim of this study is the replacement of this simple sediment with the more complex sediment representation of the MEDUSA2 model, we keep this configuration as an alternative option for comparisons (labelled  $R_{\text{sedbox}}$ ; see Sect. 2.4 below).

Differently to the version of REcoM3 described by Gürses et al. (2023), REcoM3p contains some extensions of relevance for the planned palaeo-applications: firstly, atmo-

spheric CO<sub>2</sub> concentrations are calculated assuming that the atmosphere can be represented as a homogeneous carbon reservoir. The carbon cycle on land (continental biosphere) is not considered. Temporal changes in the atmospheric volume mixing ratio of CO<sub>2</sub> ( $X_{\text{CO}_2}$ , in ppm) then solely result from the globally integrated air–sea CO<sub>2</sub> flux, given by

$$\frac{\delta X_{\text{CO}_2}}{\delta t} = -\frac{\rho_{\text{air}}}{m_{\text{atm}}} \times 10^6 \int F_{\text{CO}_2} dA, \quad (1)$$

where  $F_{\text{CO}_2}$  (mol m<sup>-2</sup> s<sup>-1</sup>) is the regional air–sea CO<sub>2</sub> flux (calculated according to Wanninkhof, 2014),  $dA$  integrates over the ocean area,  $\rho_{\text{air}} = 0.02897 \text{ kg mol}^{-1}$  is the molar mass of dry air (from Picard et al., 2008, rounded here to four significant figures), and  $m_{\text{atm}} = 5.1352 \times 10^{18} \text{ kg}$  is the mass of the dry atmosphere (Trenberth and Smith, 2005). The factor  $10^6$  serves to convert from mol fractions to parts per million (ppm).

Secondly, a riverine source of DFe was added to the already existing two sources from dust and marine sediments. Furthermore, due to the coupling to MEDUSA2, the sedimentary source of iron can be calculated in two ways: (1) in a fixed ratio to degradation of particulate organic nitrogen (PON) in the benthic layer as described in Gürses et al. (2023, Eq. A67 in Appendix A); (2) in a fixed ratio to the diffusive flux of DIN calculated by MEDUSA2 in the coupled simulations. Elrod et al. (2004) demonstrated a clear correlation between the iron flux out of sediments and the oxidation of organic matter on shelves, with an Fe : N ratio that is much higher than typical Fe : N ratios in sinking organic matter. Under anoxic conditions in sediments, the flux of iron is increased due to the greater solubility of ferrous iron. To represent this effect, we applied a higher Fe : N ratio (3  $\mu\text{mol Fe} : 20 \text{ mmol N}$ ) for the flux of iron from the sediment to the water column than the ratio of 1  $\mu\text{mol Fe} : 30 \text{ mmol N}$  that we used for remineralization in the water column. The same Fe : N ratio is used for both methods to calculate the sedimentary input of iron. A comparison of source strengths for iron is discussed in Sect. 3.2.

Thirdly, carbon isotopes were recently implemented into REcoM3p, as described in Butzin et al. (2024). However, the implementation of carbon isotopes into MEDUSA2 is not yet finished, which is why we use REcoM3p with carbon isotopes switched off.

When coupling REcoM3 to FESOM2.1, there remain some minor tracer conservation issues that are related to the use of an unstructured grid and need to be addressed. Although small (e.g. 0.53 % kyr<sup>-1</sup> for the global Si inventory in the ocean, i.e. 0.48 Tmol Si yr<sup>-1</sup>, which is smaller than the uncertainty on most input and output fluxes to and from the ocean (Tréguer et al., 2021)), such imbalances may accumulate in an unfavourable way during simulation experiments run for tens of thousands of years and longer. We therefore included a spatially uniform mass correction at the end of each coupling cycle (every 50 model years – see below) so

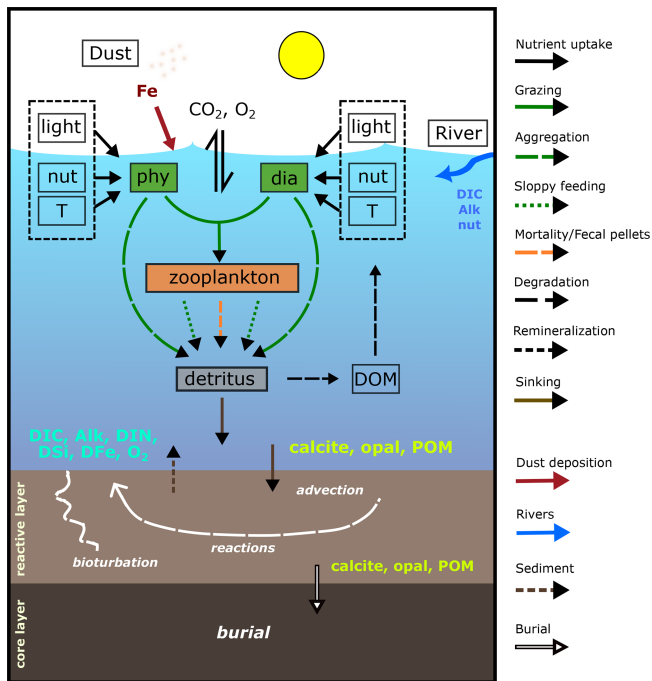


**Figure 1.** Schematic diagram of the components and interactions in REcoM3p coupled with the sediment model MEDUSA2 (modified and extended from Gürses et al., 2023, Fig. 2). Small phytoplankton (phy) and diatoms (dia) take up inorganic nutrients (nut) and grow in dependence on light and temperature ( $T$ ). One generic zooplankton consumes phytoplankton. Phytoplankton aggregation, zooplankton sloppy feeding, mortality, and fecal pellets generate sinking detritus. Sinking detritus degrades to dissolved organic matter (DOM), which then remineralizes to dissolved inorganic carbon (DIC) and nitrogen (DIN). Calcite, opal, and particulate organic matter (POM) reaching the seafloor enter the reactive layer of sediments, where accumulation, bioturbation, degradation, and dissolution take place. Dissolved products of these processes (DIC, Alk, DIN, DSi, DFe, and  $O_2$ ) go back to the bottom water by diffusion. The solids accumulate and are buried further in the core layer. Sources of DIC, Alk, and nutrients to the ocean include sediments and rivers, and dust deposition is an additional source of iron.

that the total inventory of Si is strictly conserved. A similar approach was adopted for DIC, Alk, DIN, and  $O_2$ .

### 2.1.2 The sediment model MEDUSA2

MEDUSA is a time-dependent, one-dimensional numerical model of coupled early diagenetic processes in seafloor surface sediments. The original model version (MEDUSA v1) was described in Munhoven (2007). MEDUSA v1 has evolved to become MEDUSA2, which allows a flexible chemical composition of the sediment and of the network of chemical transformations that describe the diagenetic processes (e.g. denitrification) and chemical equilibria to consider. It also offers a variety of application programming interfaces (APIs) for coupling it to ocean models with dif-

ferent grid configurations and biogeochemical components (Munhoven, 2021). Here, we provide only a general description of the MEDUSA2 configuration used in this study; for details, including the exact equations and parameter values adopted, please refer to the technical report “MEDUSA Setup and Selected Configuration Options” in the Supplement.

In MEDUSA, a sediment column is divided into three realms (the optional fourth one, a diffusive boundary layer at the sediment–water interface, was not considered here). The topmost part from the sediment surface is called REACLAY and encompasses the reactive mixed layer where solids sinking from the bottom layer of the ocean are collected. This is where chemical reactions take place. Solids are transported by bioturbation and advection resulting from the continuous deposition of new material, and solutes are transported by molecular diffusion. The second major realm is located underneath and is called CORELAY. It is made of a stack of sediment layers, typically 1 cm thick each. Here, no reactions or mixing take place: solids are buried and preserved in this realm, which builds up a synthetic sediment core. REACLAY and CORELAY are connected by a thin transitional layer (TRANLAY) which acts as a short-term (numerical) storage buffer and which can also be seen as the topmost layer of CORELAY. In the MEDUSA2 configuration used here, sediment columns (one per seafloor grid element) resolve a 50 cm thick reactive surface sediment layer on a vertical grid with 71 points to take into account diagenetic processes acting at depths greater than 10 cm, such as organic degradation by sulfate reduction. The grid point spacing is not regular but increases with depth in the sediment for a better representation of the strong subsurface solute concentration gradients. Only the uppermost 10 cm are mixed by bioturbation. There is no lateral exchange between sediment columns.

MEDUSA has already been coupled to several ocean biogeochemistry and Earth system models (Moreira Martinez et al., 2016; Kurahashi-Nakamura et al., 2020; Munhoven, 2021). Coupling to ocean models is done through so-called “applications” in the MEDUSA code. We introduced a new application `medusa-fesom-recom` which controls (1) the reading of FESOM2.1-REcoM3p input and conversion into format and units that MEDUSA requires, (2) the selection of processes and global rate parameter values for tracing the evolution of the concentrations of solids and solutes considered, and (3) the writing of the resulting diffusive solute exchange with the ocean to a file for usage by FESOM2.1-REcoM3p and the obtained burial loss of solids into the sediment core. These burial losses can be used to monitor and/or regulate oceanic mass balances of carbon, alkalinity, and the main nutrients (nitrogen and silicon).

Consistent with the input from FESOM2.1-REcoM3p, we chose a MEDUSA2 configuration with five solids (clay, calcite, opal, and two types of organic matter) and nine solute components ( $CO_2$ ,  $HCO_3^-$ ,  $CO_3^{2-}$ ,  $O_2$ ,  $NO_3^-$ ,  $H_4SiO_4$ ,  $NH_4^+$ ,

$\text{SO}_4^{2-}$ , and  $\text{HS}^-$ ). The two types of organic matter are needed to account for the variable stoichiometry in REcoM3p. Processes altering the content of solids and solutes in sediments include calcite dissolution, organic degradation by aerobic respiration, denitrification and sulfate reduction, opal dissolution, and chemical equilibria of the carbonate system in the porewaters. Manganese and iron reduction are not considered for organic matter degradation, since their contribution is negligible at the global scale (Thullner et al., 2009). REcoM3p only calculates formation and dissolution of calcite and does not represent aragonite. Correspondingly, only calcite dissolution in sediments is considered in the MEDUSA2 application `medusa-fesom-recom`.

As mentioned above, in the model setup, organic matter can become degraded through aerobic respiration and nitrate and sulfate reduction; i.e. organic matter is preserved and buried once it reaches a sediment depth which is devoid of  $\text{O}_2$ ,  $\text{NO}_3^-$ , and  $\text{SO}_4^{2-}$ . Bottom water concentrations of  $\text{O}_2$  and  $\text{NO}_3^-$  are taken from FESOM2.1-REcoM3p output, while the  $\text{SO}_4^{2-}$  concentration is derived from the bottom water salinity following Dickson et al. (2007), since FESOM2.1-REcoM3p does not explicitly represent sulfur.  $\text{NH}_4^+$  and  $\text{HS}^-$  concentrations at the sediment–water interface are set to 0 throughout the ocean (Thullner et al., 2009).

Biological components in REcoM3p have variable intracellular stoichiometry; thus the seafloor deposition fluxes of POC and PON have no fixed ratio. However, in MEDUSA2, degradation of particulate organic matter (POM) is calculated for POM classes with a fixed stoichiometry each. We therefore defined two end-member classes of POM in MEDUSA2 in which  $Q = \text{C} : \text{N}$  is fixed, with  $Q_1 = 106 : 21$  and  $Q_2 = 200 : 11$ , respectively, representing the minimum and maximum C : N ratio simulated in the seafloor deposition flux in REcoM3p. The total outgoing fluxes of PON from REcoM3p ( $F_N^0$ ) were then partitioned into two incoming contributions,  $F_N^{i1}$  and  $F_N^{i2}$ , according to

$$F_N^{i1} = \frac{Q_2 - Q}{Q_2 - Q_1} \cdot F_N^0, \quad (2)$$

$$F_N^{i2} = \frac{Q - Q_1}{Q_2 - Q_1} \cdot F_N^0, \quad (3)$$

where  $Q = F_C^0 / F_N^0$  is the ratio of the bulk POC flux ( $F_C^0$ ) to the PON flux ( $F_N^0$ ) that reaches the seafloor in REcoM3p. The carbon fluxes carried by the two POM classes are finally calculated by multiplying the nitrogen fluxes  $F_N^{i1}$  and  $F_N^{i2}$  by the respective C : N ratios:

$$F_C^{i1} = Q_1 \cdot F_N^{i1}, \quad (4)$$

$$F_C^{i2} = Q_2 \cdot F_N^{i2}. \quad (5)$$

The degradation timescale of organic matter depends on its elemental composition, i.e. the C : N ratio (Amon and Benner, 1994; Martin et al., 1987). In the water column in FESOM2.1-REcoM3p, we considered a faster remineralization of nitrogen compared to carbon with the ratio of 1.1 : 1

( $\rho_{\text{DetN}}$  and  $\rho_{\text{DetC}}$  in Gürses et al., 2023, Table A8). The rate law expression chosen for the oxic degradation of organic matter in the sediment is more complex: it is linear in the concentration of organic matter in porewaters (with separate expressions for  $[\text{POM}_1]$  and  $[\text{POM}_2]$ ) and includes a Monod-type (hyperbolic) limitation with respect to the concentration of oxygen in the porewaters ( $[\text{O}_2]$ ; Supplement Sect. S3.2). Organic matter degradation through nitrate and sulfate reduction is described in a similar way but taking into account the inhibition by oxygen (Supplement Sect. S3.3 and S3.4); organic matter oxidation by sulfate reduction is inhibited by oxygen and nitrate. We adopted a 100-fold-faster degradation rate for the low-C : N organic matter class ( $k_{\text{ox1}}$  for  $\text{POM}_1$ ) than for the high-C : N organic matter class ( $k_{\text{ox2}}$  for  $\text{POM}_2$ ) (Soetaert et al., 1996).

Besides organic matter, calcite, and opal, the simulated sediment contains an inert component, which we refer to as “clay” here for the sake of simplicity and which is ultimately of continental origin. It stems from dust particles deposited over the sea surface and from terrestrial materials transported to the oceans by rivers. In our model setup, annual mean dust deposition from Albani et al. (2014) is regarded as the oceanic clay input into sediments. This dust deposition distribution leads, however, to unrealistically low sedimentation (solid deposition) rates at seafloor depths shallower than 3000 m, typically by a factor of 20–50, but occasionally by more than 100, when compared to the empirical relationship of Middelburg et al. (1997). We therefore increased the deposition rate of lithogenic material (“clay”) by  $10^{-2.4-Z/1250} \times 0.1 \times 2650 \text{ kg m}^{-2} \text{ yr}^{-1}$ , where  $Z$  is the depth below sea level (in m), 0.1 is the volume fraction of solids close to the sediment surface (for a porosity of 0.9), and 2650 is the density of lithogenic material (in  $\text{kg m}^{-3}$ ). This way, the global distribution of seafloor sedimentation rates is in better agreement with the empirical relationship of Middelburg et al. (1997). The resulting global distribution of clay input used in this study is shown in Fig. A2.

## 2.2 Coupling REcoM3p and MEDUSA2

FESOM2.1-REcoM3p and MEDUSA2 are sequentially coupled through file exchange. Sinking fluxes of POC, PON, opal ( $\text{SiO}_2$ ), and calcite out of the bottom water boxes are saved as output files by FESOM2.1-REcoM3p and read as input files by MEDUSA2 (Fig. 1). Furthermore, MEDUSA2 requires information on temperature, salinity, and concentrations of Alk, DIC, oxygen, and nutrients in the bottommost ocean model box. Temperature and salinity enter thermodynamic calculations in the sediment model, and the bottom water concentrations are used in the calculation of diffusive fluxes between sediment and water column.

FESOM2.1-REcoM3p reads diffusive fluxes of nutrients, including DIN and DSi (or  $\text{H}_4\text{SiO}_4$ ), DIC, Alk, and oxygen from the MEDUSA2 output file (Fig. 1). DFe input from sediments is derived from the diffusive flux of DIN, using

a fixed Fe : N ratio. Other quantities that are calculated by MEDUSA2 are the permanent burial of carbon, organic matter, opal, and calcite in the sediment core. This output is used to monitor and compensate changes in the total mass balances of carbon and the other tracers in the ocean and reactive sediment. The burial loss is balanced by adding the same quantities as riverine input, which is distributed over the surface ocean in the model, by scaling it with the local river runoff from the forcing data.

## 2.3 Model setup

### 2.3.1 Model configuration

FESOM2.1 employs unstructured meshes with variable horizontal resolution. The default mesh of FESOM2.1-REcoM3 (COREII mesh) has about 127 000 surface nodes with a nominal average resolution of  $1^\circ$  and enhanced resolution in the equatorial belt and at high latitudes going up to 25 km (Gürses et al., 2023). For testing the coupling with MEDUSA2, a reduced model resolution (PI mesh) is used here, containing 3140 surface nodes, corresponding to a median horizontal resolution of 260 km (Butzin et al., 2024). This configuration reduces computational costs and simplifies simulations over the timescale of thousands of years in order to approach deep-ocean equilibrium and significant changes in marine sediments. MEDUSA2 is coupled to the bottom layers of the ocean model. Therefore, the horizontal grid within MEDUSA2 is always the same as in the ocean model.

Vertically, the ocean is divided into 47 layers, and the layer thickness ranges from 5 m in the surface to 250 m in the deep ocean. The full free-surface formulation (zstar) was used, allowing vertical movement of all layers, to ensure tracer conservation in FESOM (Scholz et al., 2019, 2022). In this study, the model was retuned for the coarser resolution by reducing the maximum thickness diffusivity of the Gent–McWilliams parameterization from  $3000 \text{ m}^2 \text{ s}^{-1}$  (used in the default FESOM2.1) to  $1000 \text{ m}^2 \text{ s}^{-1}$ .

### 2.3.2 Forcing and initial conditions

FESOM2.1 is initialized with January temperatures and salinities from the Polar Science Center Hydrographic Climatology (PHC3, updated from Steele et al., 2001) and driven by annually repeated atmospheric fields using the Corrected Normal Year Forcing Version 2.0 (CORE-NYF.v2; Large and Yeager, 2009).

The initial value of  $X_{\text{CO}_2}$  is 284.3 ppm following Meinhäusen et al. (2017). Alk and DIC are initialized from version 2 of the Global Ocean Data Analysis Project (GLODAPv2) data set (Lauvset et al., 2016), DIN and DSi are initialized from the Levitus World Ocean Atlas climatology of 2013 (Garcia et al., 2014), and oxygen is initialized from the Levitus World Ocean Atlas climatology of 2018 (Garcia

et al., 2019). The initial DFe field is based upon output from the Pelagic Interaction Scheme for Carbon and Ecosystem Studies (PISCES) model (Aumont et al., 2015), as outlined in Gürses et al. (2023).

Dust input of iron at the sea surface is calculated based on monthly averages of dust deposition by Albani et al. (2014) with a weight percentage for iron of 3.5 % and a solubility of 2 %. The riverine DFe input is based upon de Baar and de Jong (2001), who estimate that the rivers transport 26 Gmol Fe as DFe to the oceans each year. These authors assume that about 90 % of this is lost by flocculation when river water gets mixed with seawater, which reduces the actual input to the ocean to  $2.6 \text{ Gmol Fe yr}^{-1}$ . However, depending on types of catchment areas and the concomitant input of organic material which may act as a metal chelator, the river input of DFe can be significantly higher (Guieu et al., 1996; Krachler et al., 2005). We therefore tuned our model by varying the river input of DFe (assuming an upper limit of  $26 \text{ Gmol Fe yr}^{-1}$ ) to get a reasonable distribution of DFe and of the simulated biological productivity, and we finally adopted a total riverine DFe input of  $5.2 \text{ Gmol Fe yr}^{-1}$ . The river input of DFe is distributed at the sea surface by scaling with the river runoff, which is part of the CORE-NYF.v2 forcing.

## 2.4 Coupled simulations with FESOM2.1-REcoM3p-MEDUSA2

A coupled simulation starts with a spinup run with FESOM2.1-REcoM3p ( $R_{\text{spinup}}$ ), followed by the pre-charging of MEDUSA2 (Fig. 2). Subsequently, FESOM2.1-REcoM3p and MEDUSA2 are run alternately with a defined coupling frequency of 50 years ( $R_{\text{coupled}}$ ).

### 2.4.1 FESOM2.1-REcoM3p spinup run ( $R_{\text{spinup}}$ )

FESOM2.1 (without biogeochemistry) was run for 1000 years as a spinup of the ocean circulation. After that, REcoM3p was switched on and run for another 1500 years to obtain a quasi-equilibrium of deep-ocean concentrations. During these 1500 years, the exchange between ocean and sediment was calculated with the original one-layer sediment representation. Model output of the last 50 years was analysed as the initial conditions for  $R_{\text{coupled}}$  in Sect. 3.1.

### 2.4.2 Pre-charging of MEDUSA2

Continuous exchange of material between ocean and sediments alters both ocean chemical boundary conditions and the content of the reactive sediment layer. The latter changes much more slowly due to low sedimentation rates. To reduce the computing time for obtaining significant changes in sediments, MEDUSA2 was first run for 100 000 years forced by the results from  $R_{\text{spinup}}$  so that the sediment layers in MEDUSA are charged before an interactive coupled

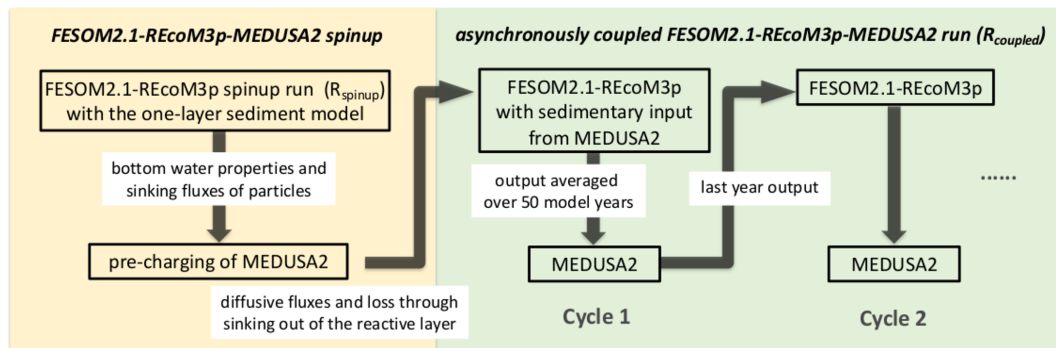


**Figure 2.** Workflow of a coupled FESOM2.1-REcoM3p-MEDUSA2 simulation.

FESOM2.1-REcoM3p-MEDUSA2 simulation starts. This way, we may reach an initial seafloor sediment distribution that is as consistent as possible with the productivity pattern, the cycling in the water column, and the boundary conditions prevailing at the seafloor (oxygenation, saturation state, etc.).

### 2.4.3 Coupled simulation ( $R_{\text{coupled}}$ )

Two simulations were started from the state of year 1500 in  $R_{\text{spinup}}$  and compared to demonstrate how carbon storage in sediments affects the marine carbon cycle and atmospheric  $\text{CO}_2$ : (1)  $R_{\text{sedbox}}$  is the continuation of  $R_{\text{spinup}}$  from year 1500 to year 3500; (2) a coupled simulation  $R_{\text{coupled}}$  was conducted for 2000 model years starting with the pre-charged MEDUSA2 sediment layers (see previous section). A coupling frequency of 50 years was consistently applied between FESOM2.1-REcoM3p and MEDUSA2. For each coupling cycle, the output of FESOM2.1-REcoM3p was averaged over 50 years before being used as input in MEDUSA2. The sediment-to-ocean fluxes (input to FESOM2.1-REcoM3p) were updated every 50 years with results from the MEDUSA2 simulation. Within one coupling cycle, the ocean–sediment exchange fluxes to be applied at each time step were kept constant. The outputs of  $R_{\text{sedbox}}$  and  $R_{\text{coupled}}$  were averaged over the last 50 years before comparison (Sect. 3.2).

### 2.4.4 Transient simulations with perturbations in atmospheric $\text{CO}_2$ ( $R_{\text{pert1k}}$ and $R_{\text{pert2k}}$ )

To demonstrate that the ocean-only setup of FESOM2.1-REcoM3p-MEDUSA2 can be used to study transient climate changes, two experiments were conducted starting from the final state of  $R_{\text{coupled}}$ , adding 1000 and 2000 PgC into the atmosphere, respectively. With those experiments, the interactions between the atmosphere, ocean, and sediment under idealized ocean acidification scenarios were examined. Both coupled experiments ( $R_{\text{pert1k}}$  and  $R_{\text{pert2k}}$ ) were run for 2000 years, and the temporal change in the atmospheric  $\text{CO}_2$  concentration and calcite content in sediments was analysed.

### 2.4.5 Performance of the coupled model

FESOM coupled with REcoM spends about 80 % of the total run time of a simulation on the tracer transport computations (Himstedt, 2023). An acceleration method was implemented for a parallel calculation of tracer advection, and, with two parallel tracer groups on 72 cores, a speedup by a factor of 1.8 was achieved for simulations with the reduced resolution using the PI mesh (Himstedt, 2023). In this study, each coupled FESOM2.1-REcoM3p-MEDUSA2 cycle (50 model years) is then completed within 7 h computation time on 72 cores, of which the MEDUSA2-related calculations require less than 5 min (i.e. of the order of 1 % only).

## 3 Results and discussion

### 3.1 FESOM2.1-REcoM3p spinup simulation with the one-layer sediment ( $R_{\text{spinup}}$ )

Generally, the global and basin-averaged profiles of DIC, Alk, DIN, DSi, and  $\text{O}_2$  in the FESOM2.1-REcoM3p spinup run ( $R_{\text{spinup}}$ ) agree well with GLODAPv2 (Large and Yeager, 2009) and WOA data (Garcia et al., 2019) (Fig. A1), particularly in ocean basins covering large areas of the open ocean. The modelled  $\text{O}_2$  concentration in the Arctic Ocean is clearly lower than observed. This will be discussed in Sect. 3.2.5 below.

The global net primary production (NPP) of  $35 \text{ PgCyr}^{-1}$  is lower than the satellite-based estimates but comparable to other modelling studies (see Gürses et al., 2023, Table 3 and references therein), e.g.  $24.5\text{--}57.3 \text{ PgCyr}^{-1}$  in CMIP6 (Séférian et al., 2020). The larger part of NPP comes from the small phytoplankton ( $23 \text{ PgCyr}^{-1}$ ); diatoms contribute the remaining  $12 \text{ PgCyr}^{-1}$ . Carbon export out of the upper 100 m into the deep ocean is  $6.6 \text{ PgCyr}^{-1}$ . The slightly higher productivity and export found here compared to an NPP of  $32.5 \text{ PgCyr}^{-1}$  in the base version of FESOM2.1-REcoM3 (Gürses et al., 2023) can be explained by the differences between the model setups:

1. There is a much coarser spatial resolution of the PI mesh used here and a different forcing data set, which result in differences in resolved physical processes (e.g. circulation and mixing) and thus in the environmental conditions for phytoplankton growth (e.g. light, temperature, and nutrient supply).
2. REcoM3p uses a configuration with a single zooplankton class, whereas the simulations in Gürses et al. (2023) contained two zooplankton classes.
3. Additional iron input from rivers relieves iron limitation of phytoplankton growth in some regions.

Deposition fluxes from the ocean bottom layer onto the top of the sediments from different simulations and burial fluxes of POC, calcite, and opal from the coupled simulation are summarized in Table 1 along with observation-based estimates. The simulated global deposition rate of POC ( $650 \text{ PgC kyr}^{-1}$ ) in  $R_{\text{spinup}}$  is lower than the range of observation-based estimates ( $930\text{--}5739 \text{ PgC kyr}^{-1}$ ) reported by Burdige (2007). This is not surprising, since the global primary and export production in our model are both lower than observations. The simulated POC deposition rates (Fig. 3a) are in the same order of magnitude as Dunne et al. (2007) but mainly occur on top of deep-sea sediments (deeper than 1 km). The contribution of the deposition rates in shallower waters (37 %) underestimates the relative share of 67 %–82 % obtained by others (Muller-Karger et al., 2005; Burdige, 2007). Models with a coarse resolution do not resolve physical processes and thus the biological recycling of carbon in shelf regions well, likely leading to an unrealistic estimation of POC sinking into and accumulating in sediments. To quantify the effect of model resolution, we performed a simulation with exactly the same model code and setup but at a higher resolution, with 126 858 surface nodes ( $R^{\text{high}}$ ), i.e. as in Gürses et al. (2023). The total POC deposition rate of  $1380 \text{ PgC kyr}^{-1}$  in  $R^{\text{high}}$  fits in the estimated range, and the flux in shallower waters represents a larger fraction (70 %) of the global flux, which falls within the range of estimates (67 %–82 %). Here, we still consider model results with a coarse resolution, which is commonly used for technical tests, allowing us to run a reasonable number of tuning experiments and coupled simulations over several thousands of years within a realistic time frame.

A total calcite deposition rate of  $380 \text{ PgC kyr}^{-1}$  is found to reach the ocean–sediment interface in  $R_{\text{spinup}}$ , from which  $370 \text{ PgC kyr}^{-1}$  happened in the deep ocean below 1 km water depth. Be aware that the omissions of aragonite and of the benthic production of  $\text{CaCO}_3$  (e.g. by coral reefs) are important shortcomings of our approach. Buitenhuis et al. (2019) simulated three pelagic calcifiers and estimated a contribution of aragonite producers to shallow-water export of  $\text{CaCO}_3$  at 100 m of at least 33 %. Furthermore, coccolithophore and calcifying zooplankton together are reported to contribute to the global carbonate fluxes by 40 %–60 %,

and the rest of the fluxes remains unexplained (Knecht et al., 2023), which also results in high uncertainty in the simulating calcifying organisms and  $\text{CaCO}_3$  fluxes. Our model roughly reproduces the spatial pattern of the Th-normalized deposition fluxes (Hayes et al., 2021), with high fluxes in the North Atlantic and Arabian Sea (up to  $2 \text{ g cm}^{-2} \text{ kyr}^{-1}$ ) and lower fluxes in large areas in the Pacific and Southern oceans ( $< 1 \text{ g cm}^{-2} \text{ kyr}^{-1}$ ; Fig. 3b). Only in some parts of the eastern equatorial Pacific region are the modelled calcite fluxes about 2 times higher than in Hayes et al. (2021), which might be caused by the overly high calcite production in this region in the model.

The seafloor deposition rate of opal in  $R_{\text{spinup}}$  is  $70 \text{ Pmol Si kyr}^{-1}$ , of which  $65 \text{ Pmol Si kyr}^{-1}$  takes place at seafloor depths greater than 1 km. Observation-based estimates available in the literature unfortunately provide a conflicting picture, with  $22\text{--}40 \text{ Pmol Si kyr}^{-1}$  for the total flux (Dunne et al., 2007; Nelson et al., 1995; Tréguer et al., 1995), while, in the ocean that is deeper than 1 km,  $84 \pm 17 \text{ Pmol Si kyr}^{-1}$  (Tréguer and De La Rocha, 2013; Tréguer et al., 2021) should settle. Assuming that the more recent data are of better quality, we conclude that the simulated opal deposition rates in the deep ocean agree well with reconstructions, while, for the total rates, a revised data set seems necessary. The spatial distribution of opal fluxes agrees qualitatively well with Hayes et al. (2021), with high fluxes at high latitudes in both hemispheres and moderate ones in the eastern equatorial Pacific (Fig. 3c). However, the model shows much higher values in the Southern Ocean, indicating that the Fe limitation of diatom growth in the Southern Ocean is too weak in the model.

During the total 1500 simulated years, the atmospheric  $\text{CO}_2$  concentration first rises with time and reaches 289 ppm at the end of  $R_{\text{spinup}}$  (Fig. 4).

## 3.2 The coupled simulation with FESOM2.1-REcoM3p-MEDUSA2 ( $R_{\text{coupled}}$ )

### 3.2.1 Sediment content

The weight percentage of sediment composition (Fig. 5) is compared in the following with the data compilation of the surface sediment composition of Hayes et al. (2021). It should be noted that the latter broadly agrees with the alternative and older compilation of Seiter et al. (2004).

Simulated calcite content in  $R_{\text{coupled}}$  (Fig. 5, top row) exhibits high values (up to  $> 80 \%$ ) in the Atlantic, the tropical and subtropical South Pacific, and the Indian Ocean and shows lower values (near zero) in the North Pacific and the Southern Ocean. Also, the calcite-rich sediments along the Mid-Atlantic Ridge are reproduced to some extent in the model. This simulated pattern generally agrees well with Hayes et al. (2021).

Opal content (Fig. 5, middle row) is elevated at high latitudes in the North Pacific and North Atlantic oceans and in



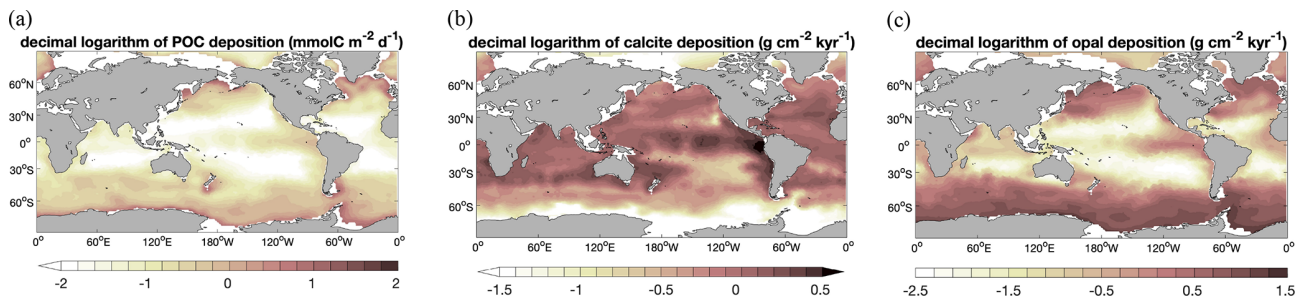
**Table 1.** Seafloor deposition and burial fluxes of POC ( $\text{PgC kyr}^{-1}$ ), calcite ( $\text{PgC kyr}^{-1}$ ), and opal ( $\text{Pmol Si kyr}^{-1}$ ) in simulations and observation-based estimates, reported for the global ocean and ocean regions deeper than 1 km.  $R^{\text{high}}$  is shown here to demonstrate the impact of model resolution on the simulated seafloor deposition, and this study rather focuses on the low-resolution simulations.

|                      | Seafloor deposition   |                       |         |        |                    |                    |
|----------------------|-----------------------|-----------------------|---------|--------|--------------------|--------------------|
|                      | POC                   |                       | Calcite |        | Opal               |                    |
|                      | Global                | > 1 km                | Global  | > 1 km | Global             | > 1 km             |
| $R_{\text{sedbox}}$  | 650                   | 410                   | 380     | 370    | 70                 | 65                 |
| $R_{\text{coupled}}$ | 420                   | 270                   | 370     | 360    | 80                 | 70                 |
| $R^{\text{high}}$    | 1380                  | 415                   | 300     | 260    | 90                 | 70                 |
| Observed             | 930–5739 <sup>a</sup> | 310–1029 <sup>b</sup> |         |        | 22–40 <sup>c</sup> | 79–84 <sup>d</sup> |

|                      | Burial                |                    |                  |                      |                  |                      |
|----------------------|-----------------------|--------------------|------------------|----------------------|------------------|----------------------|
|                      | POC                   |                    | Calcite          |                      | Opal             |                      |
|                      | Global                | > 1 km             | Global           | > 1 km               | Global           | > 1 km               |
| $R_{\text{coupled}}$ | 86                    | 28                 | 100              | 90                   | 18               | 13                   |
| Observed             | 160–2600 <sup>e</sup> | 2–300 <sup>f</sup> | 280 <sup>g</sup> | 100–150 <sup>h</sup> | 7.1 <sup>i</sup> | 5.9–9.2 <sup>j</sup> |

Reference keys are as follows. B: Burdige (2007); C16: Cartapanis et al. (2016); C18: Cartapanis et al. (2018); D07: Dunne et al. (2007); D12: Dunne et al. (2012); Ha: Hayes et al. (2021); Hi: Hilton and West (2020); J: Jahnke (1996); M: Muller-Karger et al. (2005); N: Nelson et al. (1995); Sa: Sarmiento et al. (2002); Se: Seiter et al. (2005); T95: Tréguer et al. (1995); T13: Tréguer and De La Rocha (2013); T21: Tréguer et al. (2021). <sup>a</sup> B, D07, M, Sa. <sup>b</sup> B, J, M, Sa, Se. <sup>c</sup> D07, N, T95. <sup>d</sup> J, T21. <sup>e</sup> B, C18, D07, M. <sup>f</sup> B, C16, C18, D07, Hi, Ha, J, M, Se. <sup>g</sup> C18. <sup>h</sup> C18, D12, Ha, Sa. <sup>i</sup> T95. <sup>j</sup> Ha, T13, T95, T21.



**Figure 3.** Decimal logarithm of seafloor deposition rates of (a) POC ( $\text{mmol C m}^{-2} \text{d}^{-1}$ ; i.e. the same units as in Dunne et al., 2007), (b) calcite ( $\text{g cm}^{-2} \text{kyr}^{-1}$ ), and (c) opal ( $\text{g cm}^{-2} \text{kyr}^{-1}$ ) in  $R_{\text{spinup}}$ .

the Southern Ocean at the Antarctic Polar Front. This is also seen in the data compilation. The opal distribution mainly reflects the diatom productivity (Fig. 6a) and opal deposition rates (Fig. 3). The latter has a similar pattern to  $^{230}\text{Th}$ -normalized estimates by Hayes et al. (2021), whereas much higher fluxes are found in the model over large areas in the Southern Ocean. This could lead to a likely overestimation of opal content in sediments, although not many observations are available for these areas. The opal belt in the eastern equatorial Pacific is smaller and less pronounced in the model than observed. This is related to the somewhat overly strong iron limitation of diatoms in this region in our model.

Simulated sediment TOC (Fig. 5, bottom row) is elevated at high latitudes in the Atlantic, North Pacific, and Southern oceans, similarly to opal. Also, significantly higher TOC preservation is found in the eastern equatorial Pacific. Be-

sides the contribution by diatoms, small phytoplankton in the model also have a high productivity in this region (Fig. 6b). Only a small amount of TOC is present in sediments in large areas of the open ocean. The global pattern of sediment TOC content roughly agrees with data compilation, although a detailed comparison of POC content in the Southern Hemisphere, particularly in the South Pacific Ocean, is not possible due to lack of data. The magnitude of TOC preservation in shallow waters and upwelling regions is somewhat lower compared to data compilation. This may in part be explained by the fact that the modelled biological production and thus the deposition flux to sediments are both lower than observation-based estimates (Sect. 3.1).

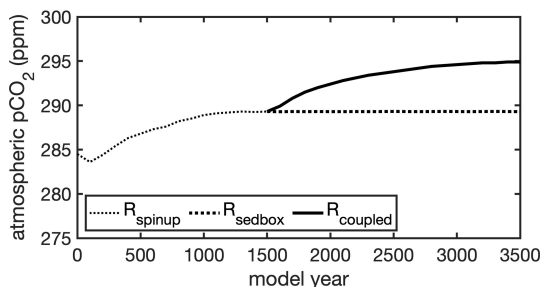


**Figure 4.** Simulated atmospheric  $\text{CO}_2$  during 3500 model years: a FESOM2-REcoM3p spinup simulation with an integrated one-layer sediment ( $R_{\text{spinup}}$ ) was run for 1500 years; after 1500 years, the model with an integrated one-layer sediment was run for further a 2000 years ( $R_{\text{sedbox}}$ ) and a simulation coupled with MEDUSA2 ( $R_{\text{coupled}}$ ) was branched off and run for 2000 years.

### 3.2.2 Degradation of organic matter in sediments

Three different pathways of degradation of organic matter in sediments are considered here: aerobic respiration, nitrate reduction, and sulfate reduction. This setup offers the possibility to have a closer look at their roles in different ocean regions. Figure 7 shows the logarithm of organic carbon degradation rate ( $\mu\text{molC cm}^{-2} \text{yr}^{-1}$ ) by aerobic respiration (a), nitrate reduction (b), and sulfate reduction (c) integrated over the upper sediment layers of 10 cm. Aerobic respiration and denitrification roughly follow the pattern of POC deposition flux (Fig. 3a), while sulfate reduction mainly concentrates in much smaller areas at high latitudes and some upwelling regions with high biological productivity. In large areas of the deep-sea sediments, aerobic respiration is the dominant degradation process. Nitrate reduction has lower rates than aerobic respiration in most regions of the world ocean, except for the high-latitude North Pacific, where porewater oxygen is fully consumed through organic matter degradation. In high-latitude regions, high rates of sulfate reduction reach up to 2 orders of magnitude compared to those of the other two processes.

Globally in the modelled 50 cm reactive sediment layer, about  $33 \text{ TmolC yr}^{-1}$  is remineralized, where 45 % is contributed by aerobic respiration, 9 % is contributed by nitrate, and 46 % is contributed by sulfate reduction. Our total carbon remineralization is comparable to Sarmiento and Gruber (2006) ( $\sim 27 \text{ TmolC yr}^{-1}$ ), while previously reported data-based estimates and model results cover a large range from 19 to  $260 \text{ TmolC yr}^{-1}$  (Thullner et al., 2009; Burdige, 2007; Smith and Hollibaugh, 1993; Jørgensen, 1983).

Aerobic respiration of  $15 \text{ TmolC yr}^{-1}$  falls below the range of estimates based on oxygen consumption ( $33\text{--}97 \text{ TmolC yr}^{-1}$ ) for deep-sea sediments ( $> 1000 \text{ m}$ ) (Jahnke, 1996; Christensen, 2000; Andersson et al., 2004; Seiter et al., 2005; Glud, 2008; Jørgensen et al., 2022) and is much lower than estimates for the global sediments ( $99\text{--}212 \text{ TmolC yr}^{-1}$ ;

see Snelgrove et al., 2018; Stratmann et al., 2019; Jørgensen et al., 2022) but substantially higher than some model results (e.g.  $3.1 \text{ TmolC yr}^{-1}$  by Thullner et al., 2009).

Denitrification removes about  $2.9 \text{ TmolN yr}^{-1}$ , which is within the range of previous estimates of  $1\text{--}12 \text{ TmolN yr}^{-1}$  (DeVries et al., 2013; Thullner et al., 2009; Liu and Kaplan, 1984; Hattori, 1983; Jørgensen, 1983; Codispoti and Christensen, 1985; Christensen, 1994; Christensen et al., 1987) but lower than the range of  $16\text{--}20 \text{ TmolN yr}^{-1}$  of Middelburg et al. (1996).

Sulfate reduction accounts for 46 % of the global carbon mineralization rate in our model, within the range between 30 %–76 % reported in previous studies (Canfield et al., 2005; Jørgensen and Kasten, 2006; Thullner et al., 2009). The highest values of sulfate reduction are around  $400 \mu\text{molC cm}^{-2} \text{yr}^{-1}$ , in line with the data compilation by Middelburg et al. (1997) for sediments in shallower waters.

### 3.2.3 Solute exchange across the sediment–water interface

The diffusive flux of DIC from the sediment to the ocean shows a similar pattern to DIN, with high fluxes in regions with high input of organic matter into sediments (Fig. 8a and c). One exception for DIN is the net flux of DIN from the ocean into the sediment in regions along the Pacific coasts. In Fig. 7, these regions are characterized by high rates of denitrification, which results in a substantial reduction in DIN in the porewater and thus a net diffusion of DIN from the ocean bottom water to the sediment.

Diffusive fluxes of  $\text{O}_2$  show more or less the opposite pattern to DIC. In regions where the seafloor deposition rate of organic matter is high (Fig. 8d), e.g. in the Northern Hemisphere around  $60^\circ$  or in the Southern Ocean, degradation of organic matter leads to a high  $\text{O}_2$  flux from the ocean to the sediments and a high DIC flux from the sediment to the ocean.

The Alk flux distribution (Fig. 8b) looks more complex and is the result of two processes that have opposite effects: degradation of organic matter decreases the alkalinity in porewater, while calcite dissolution increases it. Therefore, in those regions where the organic matter degradation rate in the surface sediment is high (i.e. where  $\text{O}_2$  uptake is high; Fig. 8d), alkalinity in porewaters may get lowered to the extent that there is a net influx of alkalinity from the ocean bottom water to the sediment. In the Atlantic Ocean, the Indian Ocean, and parts of the Pacific Ocean where calcite inputs to the sediment are high, alkalinity in porewater is clearly increased and there is a net diffusive flux of alkalinity out of the sediment into the ocean bottom water.

### 3.2.4 Burial fluxes out of the reactive layer

The simulated POC burial flux in the global sediment ( $86 \text{ PgC kyr}^{-1}$ ) is lower than the observed range ( $160\text{--}$

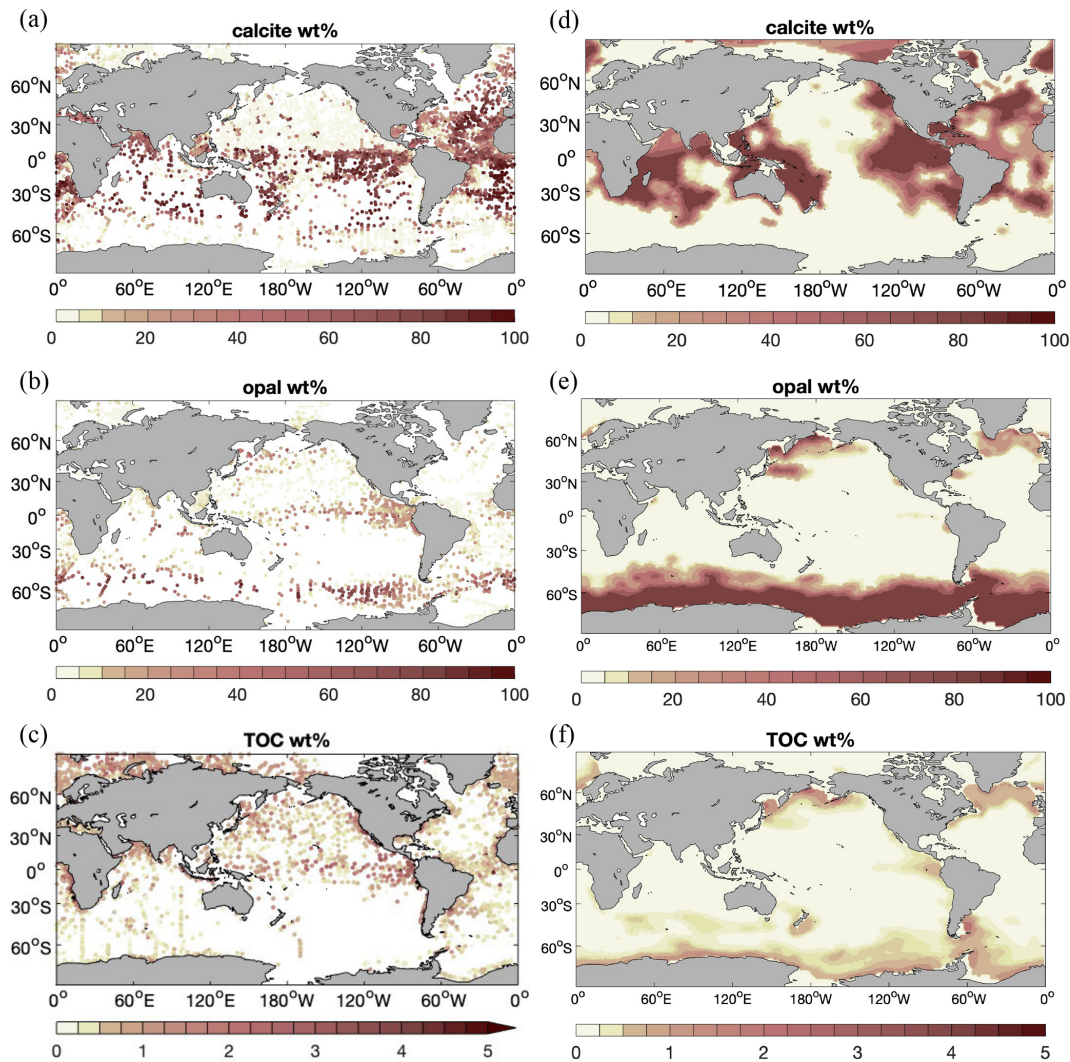


**Figure 5.** Distribution (wt %) of (a, d) calcite, (b, e) opal, and (c, f) total particulate organic carbon (TOC) in the sediment, averaged over the upper 10 cm of sediments. (a–c) Data compilation of averages over the Holocene age and measurements reported for the surface sediment by Hayes et al. (2021); (d–f) results from simulation  $R_{\text{coupled}}$ .

2600 PgC kyr<sup>-1</sup>; Table 1), consistent with the comparison for the productivity and sinking fluxes. In the deep-sea sediments, the simulated flux (28 PgC kyr<sup>-1</sup>) is within but close to the lower end of the observed range (2–300 PgC kyr<sup>-1</sup>), reflecting again the inability of our model to represent shallow-water processes with the current resolution.

Similarly, the simulated global burial flux of CaCO<sub>3</sub> (100 PgC kyr<sup>-1</sup>) is much lower than the observation-based estimate (280 PgC kyr<sup>-1</sup>), while the deep-sea burial of 95 PgC kyr<sup>-1</sup> is close to the lower end of the observed range of 100–150 PgC kyr<sup>-1</sup>. The observation-based estimates suggest a roughly equal distribution between shallow and deep-sea environments, while the model simulates only about 5 % of the global calcite burial in sediments at depths shallower than 1 km. The possible cause is the omission of some

CaCO<sub>3</sub> producers in REcoM3p, which was already discussed in Sect. 3.1.

The simulated opal burial in deep-sea sediments (13 Pmol Si kyr<sup>-1</sup>) exceeds the observed range (5.9–9.2 Pmol Si kyr<sup>-1</sup>), reflecting an overestimation of opal deposition in large areas in the Southern Ocean. It is difficult to compare the modelled global burial of 18 Pmol Si kyr<sup>-1</sup> with the only available but relatively old estimate of 7.1 Pmol Si kyr<sup>-1</sup> by Tréguer et al. (1995), which is even lower than other estimates for the deep-sea burial. This issue was already mentioned in the discussion of opal deposition flux in Sect. 3.1.

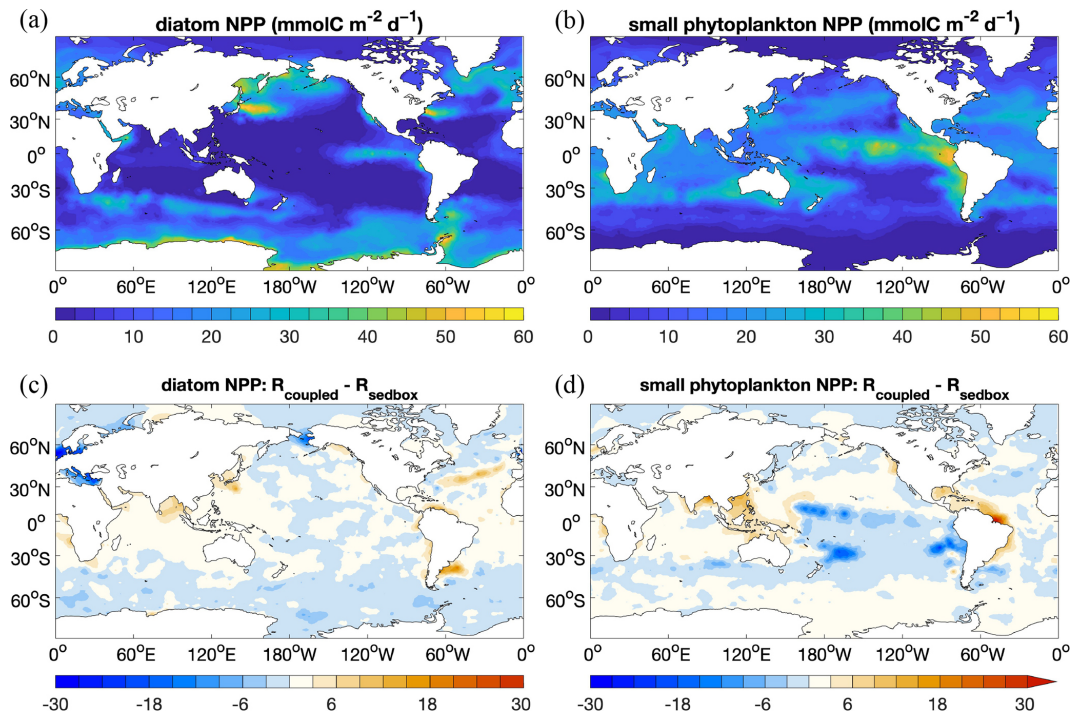


**Figure 6.** NPP ( $\text{mmolC m}^{-2} \text{d}^{-1}$ ) of (a) diatoms and (b) small phytoplankton in  $R_{\text{sedbox}}$  and (c, d) the difference in NPP between the two simulations ( $R_{\text{coupled}} - R_{\text{sedbox}}$ ).

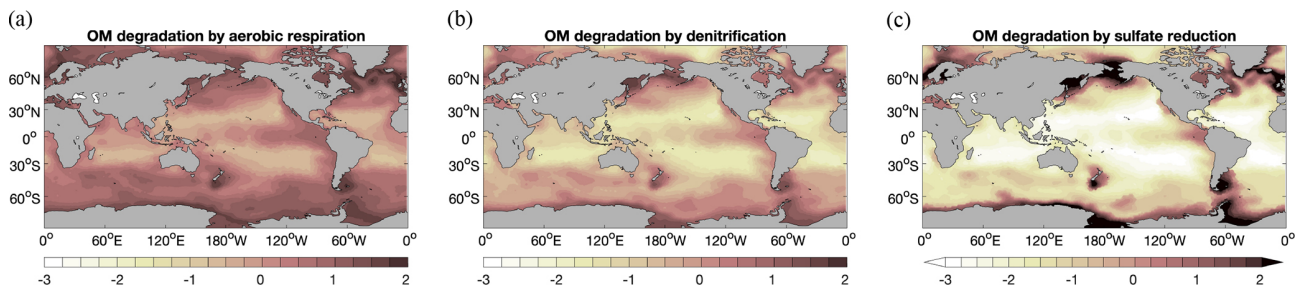


**Figure 7.** Decimal logarithm of organic carbon degradation rates ( $\mu\text{molC cm}^{-2} \text{yr}^{-1}$ ) by aerobic respiration (a), denitrification (b), and sulfate reduction (c). The rates are vertically integrated over the top 10 cm of the modelled reactive sediment layer, i.e. the mixed layer.

### 3.2.5 Impact of the complex sediment on productivity and nutrient supply

The globally averaged vertical distributions of DIC, Alk,  $\text{O}_2$ , and nutrients do not differ much between  $R_{\text{sedbox}}$  (Fig. A1) and  $R_{\text{coupled}}$  (Fig. 9). The  $\text{O}_2$  distribution in the Arctic Ocean is considerably improved in  $R_{\text{coupled}}$ . In MEDUSA2, the oxic degradation rate of organic matter depends on the  $\text{O}_2$  concentration in the sediment, whereas, in the one-layer sediment model,  $\text{O}_2$  consumption in sediments is calculated with a fixed  $\text{O}_2 : \text{C}$  ratio and subtracted from the bottom water  $\text{O}_2$  concentration, likely leading to an overestimation of degradation of organic matter and the lowering of  $\text{O}_2$  concentrations in the bottom water. This also applies to other regions with high deposition of organic matter, such as the Southern

Ocean and parts of the Pacific Ocean, which also show small improvements in the  $\text{O}_2$  profiles.

The marine NPP in the coupled simulation  $R_{\text{coupled}}$  is nearly the same as in  $R_{\text{sedbox}}$ . The spatial distribution of NPP differences between the two simulations (Fig. 6) reveals higher productivity by both diatoms and small phytoplankton in coastal regions with large riverine nutrient inputs (DIN and DSi; Fig. 10c and d), which were not considered for  $R_{\text{sedbox}}$ .

Nutrient supply in the simulations using MEDUSA2 or the one-layer sediment differs in two ways. Firstly, the total diagenetic flux of nutrients from the sediment to the ocean is lower when using MEDUSA2 (Fig. 10a and b; Table 2), since particles sinking into sediment can be stored there: a part is degraded or dissolved in the reactive layer and the remineralization products released to the porewaters from where they

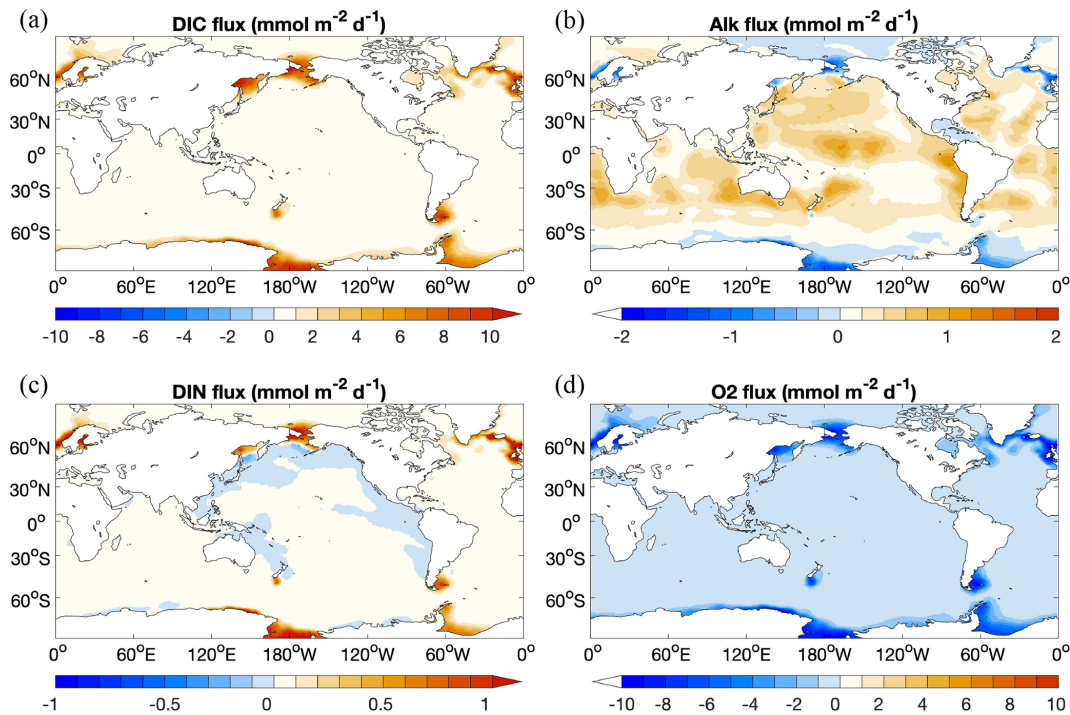


**Figure 8.** Diffusive flux of (a) DIC, (b) Alk, (c) DIN, and (d) O<sub>2</sub> from the sediment to the ocean ( $\text{mmol m}^{-2} \text{d}^{-1}$ ). Sources for the ocean are shown as positive values.

may diffuse back to the overlying ocean bottom waters, while the rest is buried in the deeper core layers (Munhoven, 2021). Storage and burial delay nutrient recycling and reduce the sedimentary nutrient source when compared to the full degradation and dissolution, which takes place in the single-layer sediment. Secondly, the current riverine source of nutrients considered in the coupled simulation is estimated from the solid burial flux that leaves the reactive sediment layer to be transferred to the core layer in MEDUSA2. This additional source brings nutrients directly into surface waters near river mouths (Fig. 10c and d). As a result, diatom productivity shows a clear decrease in the North Sea and the Bering Sea (Fig. 6c), where DIN, DSi, and DFe from sediments are all significantly reduced (Fig. 10a and b) and no riverine input can cover the loss (Fig. 10c and d).

In  $R_{\text{coupled}}$ ,  $16.8 \text{ TmolSi yr}^{-1}$  is delivered by rivers, while the sedimentary source only decreases from  $73.2 \text{ TmolSi yr}^{-1}$  in  $R_{\text{sedbox}}$  to  $62.9 \text{ TmolSi yr}^{-1}$  (Table 2). On the other hand, the riverine input of  $0.1 \text{ TmolN yr}^{-1}$  cannot compensate the decline in the sediment input from  $8.1$  to  $5.0 \text{ TmolN yr}^{-1}$ . The nutrients supplied by rivers are, however, directly available for phytoplankton living in surface waters and can still induce phytoplankton growth in areas adjacent to river mouths (Fig. 6c and d), particularly in regions where sedimentary input does not change much (e.g. tropical and subtropical regions). The sedimentary source of iron strongly decreases as well (Table 2); however, the intensity of iron limitation for phytoplankton does not

change significantly, since the riverine source is much higher and covers most of the regions where sedimentary input becomes smaller in  $R_{\text{coupled}}$ .

### 3.2.6 Impact of the complex sediment representation on atmospheric CO<sub>2</sub> and carbon storage

The oceanic carbon pools evolved towards equilibrium concentrations during  $R_{\text{coupled}}$  by adjusting the gas exchange and the fluxes between ocean and sediment. The atmospheric CO<sub>2</sub> in  $R_{\text{coupled}}$  increased to 295 ppm after 2000 years, which is higher than the pre-industrial value of 284.3 ppm used to initialize the model but consistent with the climate state determined by the CORE-NYF.v2 forcing. The air–sea gas exchange is not completely balanced at the end of the run, with a net positive CO<sub>2</sub> flux from the atmosphere to the ocean of  $0.3 \text{ TmolC yr}^{-1}$  (Table 2), indicating that the atmosphere–ocean–sediment system has not yet reached its equilibrium. This can be seen in the temporal development of CO<sub>2</sub> (Fig. 4) and change in fluxes into and out of the sediment over time (Fig. A3).

We quantified the size of the carbon storage in the reactive sediment layer at the end of  $R_{\text{coupled}}$ , being aware of that the system is still in a transient state. Compared to  $R_{\text{sedbox}}$ , the ocean contains about 150 Pg less DIC. About 1390 PgC is accumulated in the sediment surface layer in  $R_{\text{coupled}}$ , mainly as calcite but with a 10 % contribution from POC (Table 3). Emerson and Hedges (1988) estimated a

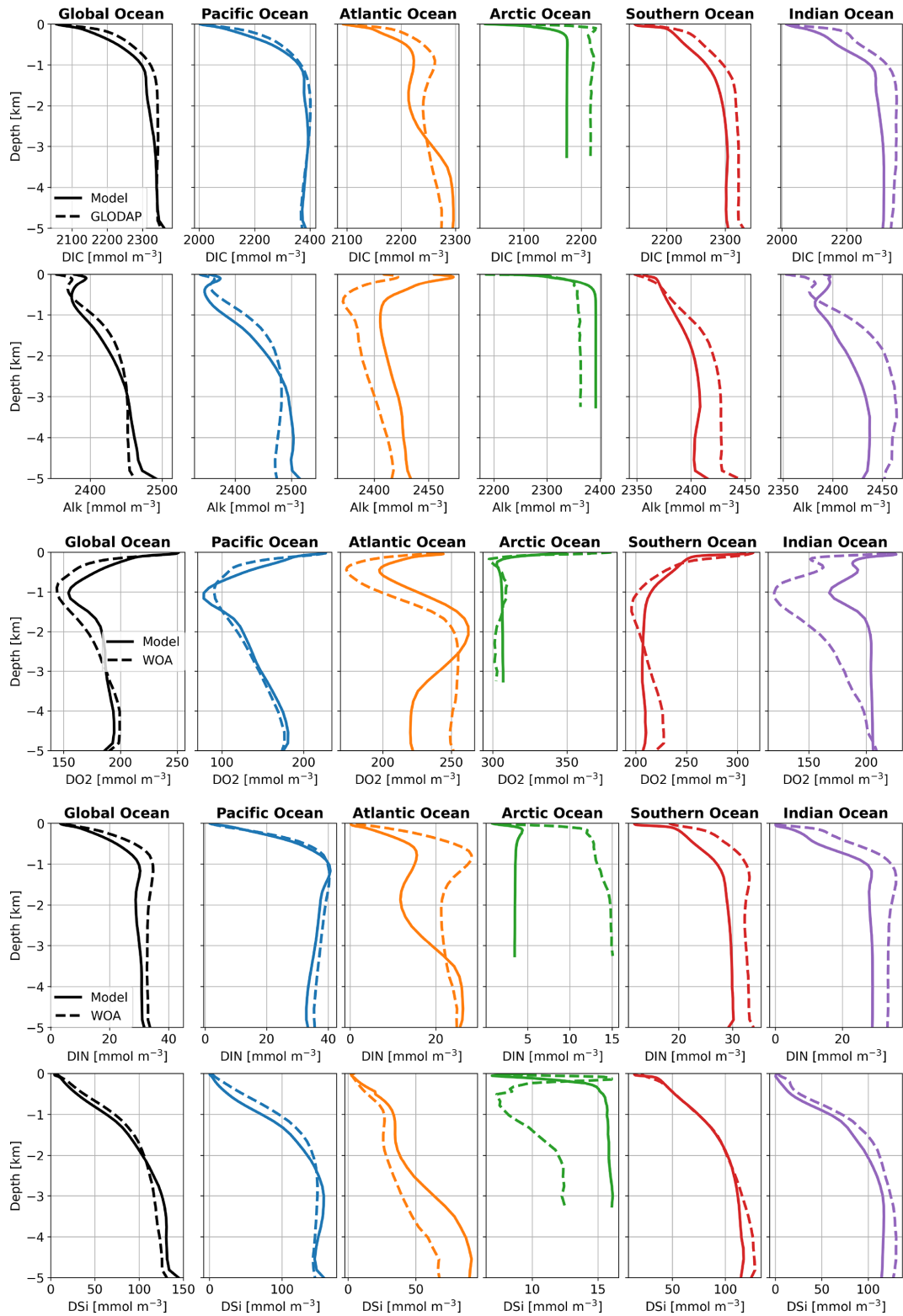


**Figure 9.** Averaged vertical profiles of DIC, Alk, O<sub>2</sub>, DIN, and DSi in ocean basins (mmol m<sup>-3</sup>) in  $R_{\text{coupled}}$  compared with GLODAP and WOA data, which were used as initial conditions in simulations in this study.

**Table 2.** Fluxes averaged over the last 50 years of the simulations. Diffusive flux of iron from sediments to the ocean is derived from the diffusive flux of DIN, using a fixed Fe : N ratio. Burial flux is calculated for the bottom of the reactive sediment layer at 50 cm. Positive fluxes are into the ocean or into sediments. Note that the units here are  $\text{Tmol yr}^{-1}$ , not  $\text{Pg yr}^{-1}$ .

|                                  | Ocean balance                                | $R_{\text{sedbox}}$ | $R_{\text{coupled}}$ |
|----------------------------------|--|---------------------|----------------------|
| C<br>( $\text{Tmol yr}^{-1}$ )   | Riverine input                               | 0                   | +9.0                 |
|                                  | Diffusive flux out of sediment               | +85.8               | +52.9                |
|                                  | Seafloor deposition (POC)                    | -54.2               | -35.5                |
|                                  | Seafloor deposition (Calc)                   | -31.5               | -30.9                |
|                                  | Air-sea gas exchange                         | -0.2                | +0.3                 |
|                                  | Sediment balance                             |                     |                      |
|                                  | Seafloor deposition (POC)                    | +54.2               | +35.5                |
|                                  | Seafloor deposition (Calc)                   | +31.5               | +30.9                |
|                                  | Diffusive flux out of sediment               | -85.8               | -52.9                |
|                                  | Burial (POC)                                 | 0                   | -1.9                 |
|                                  | Burial (Calc)                                | 0                   | -7.1                 |
| Alk<br>( $\text{Tmol yr}^{-1}$ ) | Ocean balance                                |                     |                      |
|                                  | Riverine input                               | 0                   | +14.0                |
|                                  | Diffusive flux out of sediment               | +47.9               | +41.8                |
|                                  | Seafloor deposition (PON)                    | +9.0                | +5.6                 |
|                                  | Seafloor deposition (Calc)                   | -62.9               | -61.8                |
|                                  | Sediment balance                             |                     |                      |
|                                  | Seafloor deposition (PON)                    | -9.0                | -5.6                 |
|                                  | Seafloor deposition (Calc)                   | +62.9               | +61.8                |
|                                  | Diffusive flux out of sediment               | -47.9               | -41.8                |
|                                  | Burial (POM)                                 | 0                   | +0.1                 |
|                                  | Burial (Calc)                                | 0                   | -14.1                |
| N<br>( $\text{Tmol yr}^{-1}$ )   | Ocean balance                                |                     |                      |
|                                  | Riverine input                               | 0                   | +0.1                 |
|                                  | Diffusive $\text{NO}_3$ flux out of sediment | +8.1                | +5.0                 |
|                                  | Seafloor deposition                          | -8.0                | -5.2                 |
|                                  | Sediment balance                             |                     |                      |
|                                  |  | Seafloor deposition | +8.0                 |
|                                  | Diffusive $\text{NO}_3$ flux out of sediment | -8.1                | -5.0                 |
|                                  | Burial (PON)                                 | 0                   | -0.1                 |
| Si<br>( $\text{Tmol yr}^{-1}$ )  | Ocean balance                                |                     |                      |
|                                  | Riverine input                               | 0                   | +16.8                |
|                                  | Diffusive flux out of sediment               | +73.2               | +62.9                |
|                                  | Seafloor deposition                          | -72.4               | -80.4                |
|                                  | Sediment balance                             |                     |                      |
|                                  |  | Seafloor deposition | +72.4                |
|                                  | Diffusive flux out of sediment               | -73.2               | -62.9                |
|                                  | Burial (opal)                                | 0                   | -16.8                |
| Fe<br>( $\text{Gmol yr}^{-1}$ )  | Dust   | +5.8                | +5.8                 |
|                                  | Rivers                                       | +5.2                | +5.2                 |
|                                  | Diffusive flux out of sediment               | +1.2                | +0.3                 |

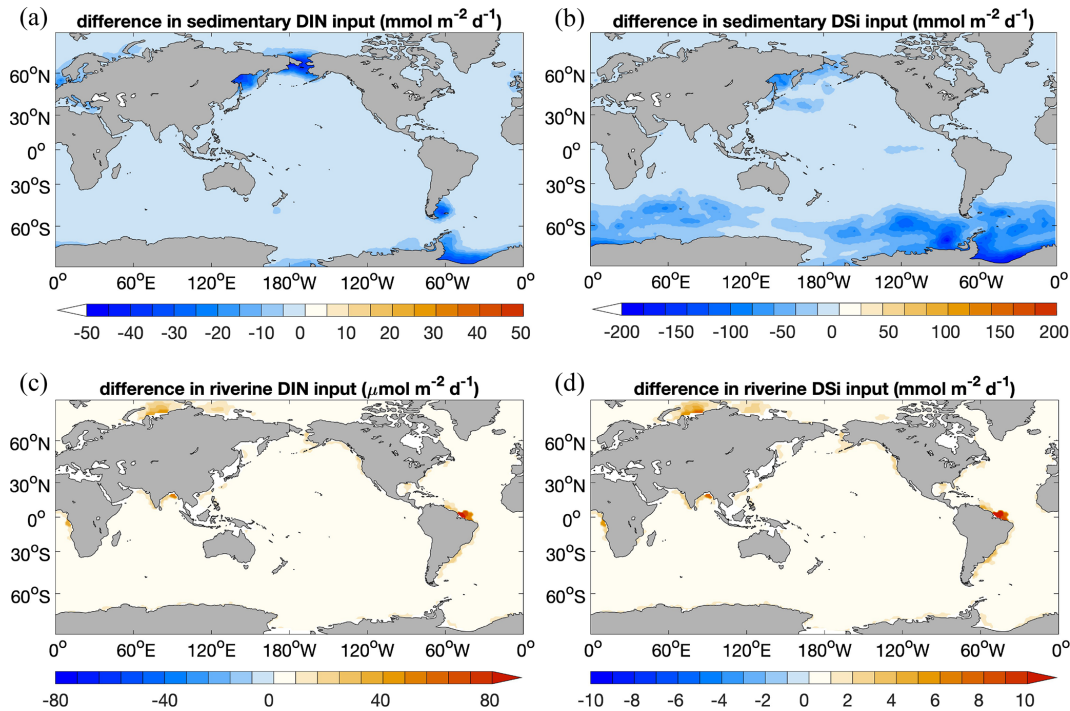


**Figure 10.** Decrease in sedimentary input of (a) DIN ( $\text{mmol m}^{-2} \text{d}^{-1}$ ) and (b) DSi ( $\text{mmol m}^{-2} \text{d}^{-1}$ ) in  $R_{\text{coupled}}$  compared to  $R_{\text{sedbox}}$ ; additional riverine input of (c) DIN ( $\mu\text{mol m}^{-2} \text{d}^{-1}$ ) and (d) DSi ( $\text{mmol m}^{-2} \text{d}^{-1}$ ) in coupled simulations  $R_{\text{coupled}}$  ( $\text{mmol m}^{-2} \text{d}^{-1}$ ). The change in sedimentary input of DFe has an identical spatial pattern to DIN, since the iron source is calculated based on the DIN source with a constant Fe : N ratio.

POC storage of 150 PgC in the mixed layer of sediments, and Parameswaran et al. (2024) recently reported that their modelled upper 10 cm of oceanic sediments harbours approximately 171 Pg TOC, while Archer (1996) reported that 800 PgC is stored as calcium carbonate within the 10 cm thick bioturbated layer. Our simulated carbon storage in the surface sediment (130 PgC as POC and 1060 PgC as calcite) is comparable with these observation- and model-based estimates. In  $R_{\text{sedbox}}$ , POC and calcite are almost completely degraded and dissolved in the single-layer sediment; thus the reservoir sizes of carbon in the sediment are close to zero.

The slow increase in atmospheric  $\text{CO}_2$  is mainly explained by the long-term storage of material in the sediments combined with the riverine input of carbon and alkalinity, which subsequently determines how DIC is distributed into its three species,  $\text{CO}_2$ ,  $\text{HCO}_3^-$ , and  $\text{CO}_3^{2-}$ , from which only  $\text{CO}_2$  can exchange with the atmosphere (Zeebe and Wolf-Gladrow, 2001).

### 3.2.7 Response of the coupled ocean–sediment system to perturbations in atmospheric $\text{CO}_2$

In the beginning of the two perturbation experiments  $R_{\text{pert1k}}$  and  $R_{\text{pert2k}}$ , 1000 and 2000 PgC were added into the atmosphere by increasing  $\text{CO}_2$  concentrations to 765 and

**Table 3.** Carbon stocks (PgC) in the ocean–sediment system in our two simulations, averaged over the last 50 years.

| Reservoir        | $R_{\text{sedbox}}$ | $R_{\text{coupled}}$ | Data                |
|------------------|---------------------|----------------------|---------------------|
| DIC              | 35 570              | 35 420               | 37 100 <sup>a</sup> |
| DOC              | 650                 | 650                  | 662 <sup>b</sup>    |
| POC              | 2                   | 2                    | 3 <sup>a</sup>      |
| Sediment POC     | < 1                 | 130                  | 150 <sup>c</sup>    |
| Sediment calcite | < 1                 | 1060                 | 800 <sup>d</sup>    |
| Sediment total   | < 1                 | 1390                 |                     |

<sup>a</sup> Ciais et al. (2013), pre-industrial estimate. <sup>b</sup> Hansell et al. (2009).

<sup>c</sup> Emerson and Hedges (1988). <sup>d</sup> Archer (1996).

1235 ppm, respectively (Fig. 11a). The ocean and sediment were initialized from the final state of  $R_{\text{coupled}}$ .

During the first 250 years,  $\text{CO}_2$  concentrations sink rapidly to  $\sim 480$  and 760 ppm, accompanied by a strong increase in DIC and initially a lesser one of alkalinity in the ocean. Afterwards, a much slower decline continues to the end of 2000 years. After 1000 years, about 23 % of the added  $\text{CO}_2$  remains in the atmosphere in  $R_{\text{pert1k}}$  and 28 % remains in  $R_{\text{pert2k}}$ , consistent with the range of 15 %–30 % reported by Archer and Brovkin (2008).

The temporal evolution of sedimentary calcite stocks in the three major ocean basins reflects the carbonate compen-



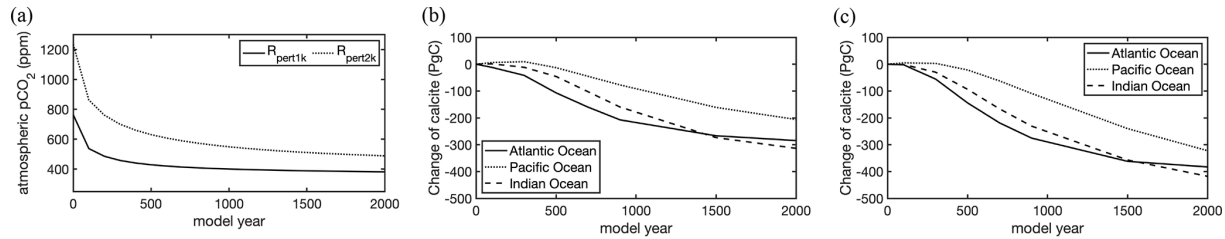


**Figure 11.** Temporal evolution of the atmospheric  $p\text{CO}_2$  in the experiments with an addition of 1000 ( $R_{\text{pert}1\text{k}}$ ) and 2000  $\text{PgC}$  ( $R_{\text{pert}2\text{k}}$ ) in the atmosphere (a) and the change in calcite content in sediments relative to the state before the  $\text{CO}_2$  perturbation in  $R_{\text{pert}1\text{k}}$  (b) and  $R_{\text{pert}2\text{k}}$  (c).

sation feedback simulated with the coupled ocean–sediment model (Fig. 11b and c). The sedimentary calcite dissolution spreads along the ocean conveyor belt. After the perturbation, inventories quite rapidly start to decline in the Atlantic Ocean, followed with some delay by the Indian Ocean, while they remain more or less stable in the Pacific Ocean for a few centuries before they also start to decline there. Losses then become stronger between 250 and 1000 years after the perturbation. By year 1000 of the simulation, the net dissolution rate already starts to subside, first in the Atlantic Ocean and somewhat more slowly in the Indian and Pacific oceans. At that time, the total carbonate losses from the sediments in  $R_{\text{pert}1\text{k}}$  amount to 220  $\text{PgC}$  in the Atlantic Ocean, 180  $\text{PgC}$  in the Indian Ocean, and 90  $\text{PgC}$  in the Pacific Ocean (total: 490  $\text{PgC}$ ); in  $R_{\text{pert}2\text{k}}$ , the total loss is 655  $\text{PgC}$ , with the same partitioning between the ocean basins as in  $R_{\text{pert}1\text{k}}$ . In both experiments, the calcite loss in the Indian Ocean becomes greater than that in the Atlantic Ocean around the year 1500. After 2000 years, the total amounts of calcite dissolved from the seafloor sediments are 800  $\text{PgC}$  in  $R_{\text{pert}1\text{k}}$  and 1120  $\text{PgC}$  in  $R_{\text{pert}2\text{k}}$ . The sedimentary calcite stock in the Atlantic Ocean seems to near a minimum after 2000 years, while that in the Indian and Pacific oceans continues to decline.

#### 4 Conclusions

This paper documented the coupling of the sediment model MEDUSA2 to the marine biogeochemical model FESOM2.1-REcoM3. The coupling was realized via file exchange, and the size of the annual fluxes that exchange material between the bottom of the ocean and the sedimentary surface was updated every 50 years. Results from a coupled simulation in a coarse resolution were presented, while a simulation with a much simpler one-layer sediment was used as reference for comparisons.

The simulation with the coupled model reproduced the distribution of DIC, Alk,  $\text{O}_2$ , and nutrients found in observational data products reasonably well. Biological productivity, deposition rates of particles onto sediments, and burial fluxes are comparable to estimations made for deep-sea regions (below 1 km water depth), whereas they are underesti-

mated in shallow-water regions (shallower than 1 km) and in the eastern equatorial Pacific due to the low model resolution and some missing processes in the ecosystem model.

Nutrient supply from sediments is lower in the coupled simulation than in the simulation with the one-layer sediment, particularly for nitrogen. However, the biological pump is not significantly affected by this decrease, since it is compensated by the additional riverine input of nutrients directly into the surface ocean. Changes in these two sources of nutrients lead to small changes in distribution patterns of diatoms and small phytoplankton.

After 2000 years, atmospheric  $\text{CO}_2$  approaches a stable state at the pre-industrial level in our coupled simulation. About 130  $\text{PgC}$  is stored in sediments as POC and 1060  $\text{PgC}$  is stored as calcite. With a coupled ocean–sediment system, the model is able to simulate the carbonate compensation feedback under moderate perturbation of  $\text{CO}_2$  in the atmosphere. Although most of the conclusions here are robust, one should nevertheless be aware that the exact carbon reservoirs and rates of deposition and burial presented in this paper are still results from a transient state of the simulation: a period of 2000 years is too short for the atmosphere–ocean–sediment system to reach full equilibrium, despite the sediment being pre-charged, i.e. equilibrated with sinking fluxes from an initial ocean model run.

Our model setup, which includes MEDUSA2, is being further developed for parallel processing. With that, FESOM2.1-REcoM3p-MEDUSA2 can be run in higher spatial resolution for a better representation of shelf regions. Additionally, a version which includes carbon isotopes is under development. Furthermore, REcoM3p-MEDUSA2 will be used as part of the Earth system model AWI-ESM2 (Shi et al., 2023) to explore changes in the carbon cycle during the last glacial cycle and feedbacks in the Earth’s climate system.

Appendix A: Figures

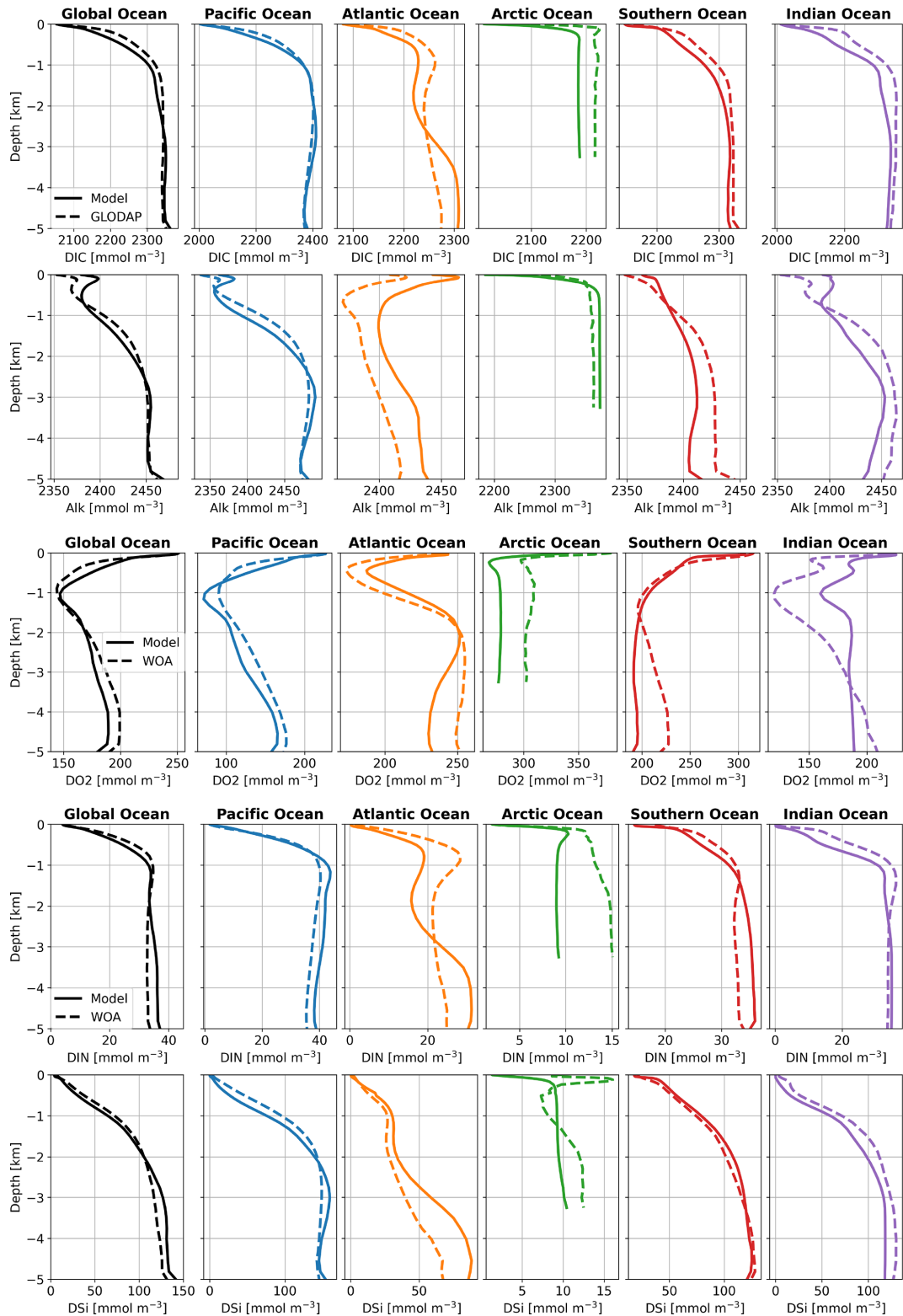


**Figure A1.** Averaged vertical profiles of DIC, Alk,  $\text{O}_2$ , DIN, and DSi in ocean basins ( $\text{mmol m}^{-3}$ ) in  $R_{\text{spinup}}$ , compared with GLODAPv2 (Large and Yeager, 2009) and WOA data (Garcia et al., 2019), which were used as initial conditions in simulations in this study.

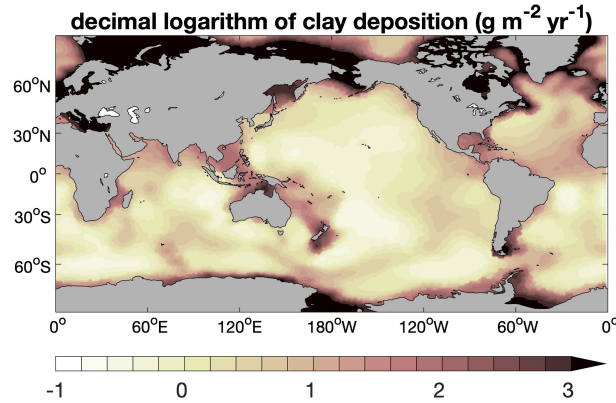


Figure A2. Decimal logarithm of clay flux at sediment–water interface ( $\text{g m}^{-2} \text{yr}^{-1}$ ).

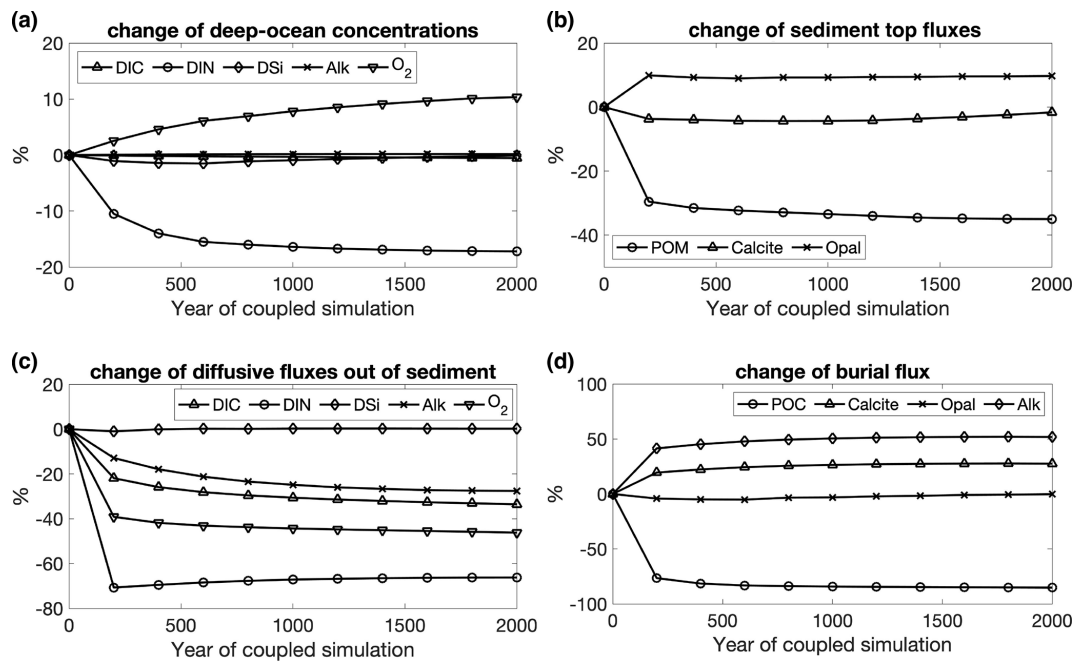


Figure A3. Temporal changes in (a) deep-ocean concentrations (DIC, DIN, DSI, Alk, and  $\text{O}_2$ ) and (c) their diffusive fluxes out of sediments; (b) deposition rates of POM, calcite, and opal onto sediment top and (d) their burial fluxes during the 2000-year coupled simulation  $R_{\text{coupled}}$ . Changes are in percentages relative to the values at the beginning of  $R_{\text{coupled}}$ .

Appendix B: FESOM2.1-REcoM3p parameters

Table B1. Parameters in REcoM3 modified in this study compared to Gürses et al. (2023).  $V_{\text{calc}}$  replaces 0.0288 in Eq. (A29) in Gürses et al. (2023).

| Parameter          | Value  | Description   | Unit            |
|--------------------|--------|---|-----------------|
| $V_{\text{det}_a}$ | 0.036  | Slope of depth-dependent sinking velocity of detritus | $\text{d}^{-1}$ |
| $V_{\text{calc}}$  | 0.0072 | Slope of depth-dependent dissolution rate of calcite  | $\text{d}^{-1}$ |

*Code and data availability.* The source code used here is archived on Zenodo (Ye, 2023, <https://doi.org/10.5281/zenodo.8315239>). The model results are available at <https://doi.org/10.5281/zenodo.14887815> (Ye, 2025).

*Supplement.* The supplement related to this article is available online at <https://doi.org/10.5194/gmd-18-977-2025-supplement>.

*Author contributions.* Conceptualization: YY, CV, GM. Data curation: YY. Formal analysis: YY, CV, GM. Funding acquisition: PK, CV, GM. Investigation: YY. Methodology: YY, CV, GM. Project administration: PK, CV. Software: YY, GM, CV, ÖG, MB. Resources: YY, CV. Supervision: CV, GM, PK. Validation: YY, CV, GM. Visualization: YY. Writing (original draft): YY. Writing (review & editing): YY and all co-authors

*Competing interests.* The contact author has declared that none of the authors has any competing interests.

*Disclaimer.* Publisher's note: Copernicus Publications remains neutral with regard to jurisdictional claims made in the text, published maps, institutional affiliations, or any other geographical representation in this paper. While Copernicus Publications makes every effort to include appropriate place names, the final responsibility lies with the authors.

*Acknowledgements.* We thank the two anonymous reviewers and the editor for their very constructive comments, which helped to improve the article a lot. Ying Ye, Peter Köhler, Christoph Völker, and Martin Butzin are supported by the German Federal Ministry of Education and Research (BMBF) through the PalMod project (grant no. 01LP1919A), which is part of the Research for Sustainability initiative (FONA; <https://www.fona.de>, last access: 14 February 2025). Ying Ye is additionally supported by the German Research Foundation (DFG; grant no. YE 170/2-1). Martin Butzin is additionally funded through DFG-ANR project MARCARA (grant no. 490763579). Financial support for Guy Munhoven's work on MEDUSA was provided by the Belgian Fund for Scientific Research – F.R.S.-FNRS (project SERENATA, grant no. CDR J.0123.19). Guy Munhoven is a Research Associate with the Belgian Fund for Scientific Research – F.R.S.-FNRS. Judith Hauck and Özgür Gürses were funded by the Initiative and Networking Fund of the Helmholtz Association (Helmholtz Young Investigator Group Marine Carbon and Ecosystem Feedbacks in the Earth System (MarESys), grant no. VH-NG-1301).

*Financial support.* This research has been supported by the Bundesministerium für Bildung und Forschung (grant no. 01LP1919A), the Fonds De La Recherche Scientifique – FNRS (grant no. CDR J.0123.19), the Helmholtz Association (grant no. VH-NG-1301), and the German Research Foundation (grant no. YE170/2-1 and

grant no. 490763579).

The article processing charges for this open-access publication were covered by the Alfred-Wegener-Institut Helmholtz-Zentrum für Polar- und Meeresforschung.

*Review statement.* This paper was edited by Sandra Arndt and reviewed by two anonymous referees.

## References

- Albani, S., Mahowald, N. M., Perry, A. T., Scanza, R. A., Zender, C. S., Heavens, N. G., Maggi, V., Kok, J. F., and Otto-Bliesner, B. L.: Improved Dust Representation in the Community Atmosphere Model, *J. Adv. Model. Earth Sy.*, 6, 541–570, <https://doi.org/10.1002/2013MS000279>, 2014.
- Amon, R. and Benner, R.: Rapid cycling of high-molecular-weight dissolved organic matter in the ocean, *Nature*, 369, 549–552, <https://doi.org/10.1038/369549a0>, 1994.
- Andersson, J. H., Wijsman, J. W. M., Herman, P. M. J., Middelburg, J. J., Soetaert, K., and Heip, C.: Respiration patterns in the deep ocean, *Geophys. Res. Lett.*, 31, L03304, <https://doi.org/10.1029/2003GL018756>, 2004.
- Archer, D. and Brovkin, V.: The Millennial Atmospheric Lifetime of Anthropogenic CO<sub>2</sub>, *Climatic Change*, 90, 283–297, <https://doi.org/10.1007/s10584-008-9413-1>, 2008.
- Archer, D., Kheshgi, H., and Maier-Reimer, E.: Multiple timescales for neutralization of fossil fuel CO<sub>2</sub>, *Geophys. Res. Lett.*, 24, 405–408, <https://doi.org/10.1029/97GL00168>, 1997.
- Archer, D., Eby, M., Brovkin, V., Ridgwell, A., Cao, L., Mikolajewicz, U., Caldeira, K., Matsumoto, K., Munhoven, G., Montenegro, A., and Tokos, K.: Atmospheric Lifetime of Fossil Fuel Carbon Dioxide, *Annu. Rev. Earth Pl. Sci.*, 37, 117–134, <https://doi.org/10.1146/annurev.earth.031208.100206>, 2009.
- Archer, D. E.: An atlas of the distribution of calcium carbonate in sediments of the deep sea, *Global Biogeochem. Cy.*, 10, 159–174, <https://doi.org/10.1029/95GB03016>, 1996.
- Aumont, O., Ethé, C., Tagliabue, A., Bopp, L., and Gehlen, M.: PISCES-v2: an ocean biogeochemical model for carbon and ecosystem studies, *Geosci. Model Dev.*, 8, 2465–2513, <https://doi.org/10.5194/gmd-8-2465-2015>, 2015.
- Broecker, W. S. and Peng, T.-H.: The role of CaCO<sub>3</sub> compensation in the glacial to interglacial atmospheric CO<sub>2</sub> change, *Global Biogeochem. Cy.*, 1, 15–29, 1987.
- Brovkin, V., Ganopolski, A., Archer, D., and Munhoven, G.: Glacial CO<sub>2</sub> cycle as a succession of key physical and biogeochemical processes, *Clim. Past*, 8, 251–264, <https://doi.org/10.5194/cp-8-251-2012>, 2012.
- Buitenhuis, E. T., Le Quéré, C., Bednaršek, N., and Schiebel, R.: Large Contribution of Pteropods to Shallow CaCO<sub>3</sub> Export, *Global Biogeochem. Cy.*, 33, 458–468, <https://doi.org/10.1029/2018GB006110>, 2019.
- Burdige, D. J.: Preservation of Organic Matter in Marine Sediments: Controls, Mechanisms, and an Imbalance in Sediment Organic Carbon Budgets?, *Chem. Rev.*, 107, 467–485, <https://doi.org/10.1021/cr050347q>, 2007.

- Butzin, M., Ye, Y., Völker, C., Gürses, Ö., Hauck, J., and Köhler, P.: Carbon isotopes in the marine biogeochemistry model FESOM2.1-REcoM3, *Geosci. Model Dev.*, 17, 1709–1727, <https://doi.org/10.5194/gmd-17-1709-2024>, 2024.
- Canfield, D. E., Kristensen, E., and Thamdrup, B.: The Sulfur Cycle, in: *Aquatic Geomicrobiology*, vol. 48 of *Advances in Marine Biology*, Elsevier, Amsterdam (NL), 313–381, [https://doi.org/10.1016/S0065-2881\(05\)48009-8](https://doi.org/10.1016/S0065-2881(05)48009-8), 2005.
- Cartapanis, O., Bianchi, D., Jaccard, S. L., and Galbraith, E. D.: Global pulses of organic carbon burial in deep-sea sediments during glacial maxima, *Nat. Commun.*, 7, 10796, <https://doi.org/10.1038/ncomms10796>, 2016.
- Cartapanis, O., Galbraith, E. D., Bianchi, D., and Jaccard, S. L.: Carbon burial in deep-sea sediment and implications for oceanic inventories of carbon and alkalinity over the last glacial cycle, *Clim. Past*, 14, 1819–1850, <https://doi.org/10.5194/cp-14-1819-2018>, 2018.
- Christensen, J. P.: Carbon export from continental shelves, denitrification and atmospheric carbon dioxide, *Cont. Shelf Res.*, 14, 547–576, 1994.
- Christensen, J. P.: A relationship between deep-sea benthic oxygen demand and oceanic primary productivity, *Oceanol. Acta*, 23, 65–82, [https://doi.org/10.1016/S0399-1784\(00\)00101-8](https://doi.org/10.1016/S0399-1784(00)00101-8), 2000.
- Christensen, J. P., Murray, J. W., Devol, A. H., and Codispoti, L. A.: Denitrification in continental shelf sediments has major impact on the oceanic nitrogen budget, *Global Biogeochem. Cy.*, 1, 97–116, 1987.
- Ciais, P., Sabine, C., Bala, G., Bopp, L., Brovkin, V., Canadell, J., Chhabra, A., DeFries, R., Galloway, J., Heimann, M., Jones, C., Quéré, C. L., Myneni, R. B., Piao, S., and Thornton, P.: Carbon and Other Biogeochemical Cycles, in: *Climate Change 2013: The Physical Science Basis. Contribution of Working Group I to the Fifth Assessment Report of the Intergovernmental Panel on Climate Change*, edited by: Stocker, T. F., Qin, D., Plattner, G.-K., Tignor, M. M. B., Allen, S. K., Boschung, J., Nauels, A., Xia, Y., Bex, V., and Midgley, P. M., Cambridge University Press, chap. 6, 465–570, [https://www.ipcc.ch/site/assets/uploads/2018/02/WG1AR5\\_Chapter06\\_FINAL.pdf](https://www.ipcc.ch/site/assets/uploads/2018/02/WG1AR5_Chapter06_FINAL.pdf) (last access: 14 February 2025), 2013.
- Codispoti, L. and Christensen, J.: Nitrification, denitrification and nitrous oxide cycling in the eastern tropical South Pacific Ocean, *Mar. Chem.*, 16, 277–300, 1985.
- de Baar, H. J. W. and de Jong, J.: Distributions, Sources and Sinks of Iron in Seawater, in: *The Biogeochemistry of Iron in Seawater*, edited by: Turner, D. R. and Hunter, K. A., vol. 7 of *IUPAC Ser. Anal. Phys. Chem. Environ. Syst.*, John Wiley & Sons, 123–253, ISBN 0-471-49068-7, 2001.
- DeVries, T., Deutsch, C., Rafter, P. A., and Primeau, F.: Marine denitrification rates determined from a global 3-D inverse model, *Biogeosciences*, 10, 2481–2496, <https://doi.org/10.5194/bg-10-2481-2013>, 2013.
- Dickson, A. G., Sabine, C. L., and Christian, J. R., eds.: *Guide to Best Practices for Ocean CO<sub>2</sub> Measurements*, vol. 3 of *PICES Special Publication, Carbon Dioxide Information and Analysis Center, Oak Ridge (TN)*, [https://www.nodc.noaa.gov/ocads/oceans/Handbook\\_2007.html](https://www.nodc.noaa.gov/ocads/oceans/Handbook_2007.html) (last access: 5 December 2004), 2007.
- Dunne, J. P., Sarmiento, J. L., and Gnanadesikan, A.: A synthesis of global particle export from the surface ocean and cycling through the ocean interior and on the seafloor, *Global Biogeochem. Cy.*, 21, GB4006, <https://doi.org/10.1029/2006GB002907>, 2007.
- Dunne, J. P., Hales, B., and Toggweiler, J. R.: Global calcite cycling constrained by sediment preservation controls, *Global Biogeochem. Cy.*, 26, GB3023, <https://doi.org/10.1029/2010GB003935>, 2012.
- Elrod, V. A., Berelson, W. M., Coale, K. H., and Johnson, K. S.: The flux of iron from continental shelf sediments: A missing source for global budgets, *Geophys. Res. Lett.*, 31, L12307, <https://doi.org/10.1029/2004GL020216>, 2004.
- Emerson, S. and Hedges, J. I.: Processes controlling the organic carbon content of open ocean sediments, *Paleoceanography*, 3, 621–634, <https://doi.org/10.1029/PA003i005p00621>, 1988.
- Friedlingstein, P., O’Sullivan, M., Jones, M. W., Andrew, R. M., Gregor, L., Hauck, J., Le Quéré, C., Luijckx, I. T., Olsen, A., Peters, G. P., Peters, W., Pongratz, J., Schwingshackl, C., Sitch, S., Canadell, J. G., Ciais, P., Jackson, R. B., Alin, S. R., Alkama, R., Arneeth, A., Arora, V. K., Bates, N. R., Becker, M., Bellouin, N., Bittig, H. C., Bopp, L., Chevallier, F., Chini, L. P., Cronin, M., Evans, W., Falk, S., Feely, R. A., Gasser, T., Gehlen, M., Gkritzalis, T., Gloege, L., Grassi, G., Gruber, N., Gürses, Ö., Harris, I., Hefner, M., Houghton, R. A., Hurtt, G. C., Iida, Y., Ilyina, T., Jain, A. K., Jersild, A., Kadono, K., Kato, E., Kennedy, D., Klein Goldewijk, K., Knauer, J., Korsbakken, J. I., Landschützer, P., Lefèvre, N., Lindsay, K., Liu, J., Liu, Z., Marland, G., Mayot, N., McGrath, M. J., Metzl, N., Monacchi, N. M., Munro, D. R., Nakaoka, S.-I., Niwa, Y., O’Brien, K., Ono, T., Palmer, P. I., Pan, N., Pierrot, D., Pockock, K., Poulter, B., Resplandy, L., Robertson, E., Rödenbeck, C., Rodriguez, C., Rosan, T. M., Schwinger, J., Séférian, R., Shutler, J. D., Skjelvan, I., Steinhoff, T., Sun, Q., Sutton, A. J., Sweeney, C., Takao, S., Tanhua, T., Tans, P. P., Tian, X., Tian, H., Tilbrook, B., Tsujino, H., Tubiello, F., van der Werf, G. R., Walker, A. P., Wanninkhof, R., Whitehead, C., Willstrand Wranne, A., Wright, R., Yuan, W., Yue, C., Yue, X., Zaehle, S., Zeng, J., and Zheng, B.: *Global Carbon Budget 2022*, *Earth Syst. Sci. Data*, 14, 4811–4900, <https://doi.org/10.5194/essd-14-4811-2022>, 2022.
- Garcia, H. E., Locarnini, R. A., Boyer, T. P., Antonov, J. I., Baranova, O. K., Zweng, M. M., Reagan, J. R., and Johnson, D. R.: *World Ocean Atlas 2013, Volume 4: Dissolved Inorganic Nutrients (Phosphate, Nitrate, Silicate)*, edited by: Levitus, S. and Mishonov, A., Tech. rep., NOAA Atlas NESDIS 76, <http://www.nodc.noaa.gov/OC5/indprod.html> (last access: 14 February 2025), 2014.
- Garcia, H. E., Weathers, K. W., Paver, C. R., Smolyar, I., Boyer, T. P., Locarnini, R. A., Zweng, M. M., Mishonov, A. V., Baranova, O. K., Seidov, D., and Reagan, J. R.: *World Ocean Atlas 2018, Volume 3: Dissolved Oxygen, Apparent Oxygen Utilization, and Oxygen Saturation*, edited by: Mishonov, A., Tech. rep., NOAA Atlas NESDIS 83, <https://www.nodc.noaa.gov/OC5/woa18/pubwoa18.html> (last access: 14 February 2025), 2019.
- Glud, R. N.: Oxygen dynamics of marine sediments, *Mar. Biol. Res.*, 4, 243–289, <https://doi.org/10.1080/17451000801888726>, 2008.
- Guieu, C., Huang, W. W., Martin, J.-M., and Yong, Y. Y.: Outflow of trace metals into the Laptev Sea by the Lena River, *Mar. Chem.*, 53, 255–267, [https://doi.org/10.1016/0304-4203\(95\)00093-3](https://doi.org/10.1016/0304-4203(95)00093-3), 1996.

- Gürses, Ö., Oziel, L., Karakuş, O., Sidorenko, D., Völker, C., Ye, Y., Zeising, M., Butzin, M., and Hauck, J.: Ocean biogeochemistry in the coupled ocean–sea ice–biogeochemistry model FESOM2.1–REcoM3, *Geosci. Model Dev.*, 16, 4883–4936, <https://doi.org/10.5194/gmd-16-4883-2023>, 2023.
- Hansell, D. A., Carlson, C. A., Repeta, D. J., and Schlitzer, R.: Dissolved Organic Matter in the Ocean : A Controversy Stimulates New Insights, *Oceanography*, 22, 202–211, <https://doi.org/10.5670/oceanog.2009.109>, 2009.
- Hattori, A.: Denitrification and dissimilatory nitrate reduction, in: Nitrogen in the marine environment, edited by: Carpenter, E. J. and Capone, D. G., chap. 6, Academic Press, New York (NY), 1st Edn., 191–232, ISBN 978-0-12-160280-2, 1983.
- Hayes, C. T., Costa, K. M., Anderson, R. F., Calvo, E., Chase, Z., Demina, L. L., Dutay, J.-C., German, C. R., Heimbürger-Boavida, L.-E., Jaccard, S. L., Jacobel, A., Kohfeld, K. E., Kravchishina, M. D., Lippold, J., Mekik, F., Missiaen, L., Pavia, F. J., Paytan, A., Pedrosa-Pamies, R., Petrova, M. V., Rahman, S., Robinson, L. F., Roy-Barman, M., Sanchez-Vidal, A., Shiller, A., Tagliabue, A., Tessin, A. C., Van Hulten, M., and Zhang, J.: Global Ocean Sediment Composition and Burial Flux in the Deep Sea, *Global Biogeochem. Cy.*, 35, e2020GB006769, <https://doi.org/10.1029/2020GB006769>, 2021.
- Hilton, R. G. and West, A. J.: Mountains, erosion and the carbon cycle, *Nat. Rev. Earth Environ.*, 1, 284–299, <https://doi.org/10.1038/s43017-020-0058-6>, 2020.
- Himstedt, K.: Multiple execution of the same MPI application to exploit parallelism at hotspots with minimal code changes: a case study with FESOM2-Iceberg and FESOM2-REcoM, *EGUsphere* [preprint], <https://doi.org/10.5194/egusphere-2023-756>, 2023.
- Hohn, S.: Coupling and decoupling of biogeochemical cycles in marine ecosystems, Ph.D. thesis, Universität Bremen, Fachbereich Biologie, 2009.
- Jahnke, R. A.: The global ocean flux of particulate organic carbon: Areal distribution and magnitude, *Global Biogeochem. Cy.*, 10, 71–88, <https://doi.org/10.1029/95GB03525>, 1996.
- Jørgensen, B. B.: Processes at the sediment–water interface, in: The Major Biogeochemical Cycles and Their Interactions, edited by: Bolin, B. and Cook, R. B., vol. 21 of SCOPE Reports, John Wiley and Sons, New York (NY), 477–509, ISBN 9780471105220, 1983.
- Jørgensen, B. B. and Kasten, S.: Sulfur Cycling and Methane Oxidation, in: Marine Geochemistry, edited by: Schulz, H. D. and Zabel, M., chap. 8, Springer-Verlag, Berlin, Heidelberg (DE), 271–309, [https://doi.org/10.1007/3-540-32144-6\\_8](https://doi.org/10.1007/3-540-32144-6_8), 2006.
- Jørgensen, B. B., Wenzhöfer, F., Egger, M., and Glud, R. N.: Sediment oxygen consumption: Role in the global marine carbon cycle, *Earth-Sci. Rev.*, 228, 103987, <https://doi.org/10.1016/j.earscirev.2022.103987>, 2022.
- Kepler, L., Landschützer, P., Gruber, N., Lauvset, S. K., and Stemmler, I.: Seasonal Carbon Dynamics in the Near-Global Ocean, *Global Biogeochem. Cy.*, 34, e2020GB006571, <https://doi.org/10.1029/2020GB006571>, 2020.
- Knecht, N. S., Benedetti, F., Hofmann Elizondo, U., Bednaršek, N., Chaabane, S., de Weerd, C., Peijnenburg, K. T. C. A., Schiebel, R., and Vogt, M.: The Impact of Zooplankton Calcifiers on the Marine Carbon Cycle, *Global Biogeochem. Cy.*, 37, e2022GB007685, <https://doi.org/10.1029/2022GB007685>, 2023.
- Köhler, P.: Anthropogenic CO<sub>2</sub> of high emission scenario compensated after 3500 years of ocean alkalization with an annually constant dissolution of 5 Pg of olivine, *Front. Climate*, 2, 575744, <https://doi.org/10.3389/fclim.2020.575744>, 2020.
- Köhler, P. and Munhoven, G.: Late Pleistocene carbon cycle revisited by considering solid Earth processes, *Paleoceanography and Paleoclimatology*, 35, e2020PA004020, <https://doi.org/10.1029/2020PA004020>, 2020.
- Krachler, R., Jirsa, F., and Ayromlou, S.: Factors influencing the dissolved iron input by river water to the open ocean, *Biogeosciences*, 2, 311–315, <https://doi.org/10.5194/bg-2-311-2005>, 2005.
- Kriest, I. and Oeschlies, A.: Swept under the carpet: organic matter burial decreases global ocean biogeochemical model sensitivity to remineralization length scale, *Biogeosciences*, 10, 8401–8422, <https://doi.org/10.5194/bg-10-8401-2013>, 2013.
- Kurahashi-Nakamura, T., Paul, A., Munhoven, G., Merkel, U., and Schulz, M.: Coupling of a sediment diagenesis model (MEDUSA) and an Earth system model (CESM1.2): a contribution toward enhanced marine biogeochemical modelling and long-term climate simulations, *Geosci. Model Dev.*, 13, 825–840, <https://doi.org/10.5194/gmd-13-825-2020>, 2020.
- Lan, X., Tans, P., and Thoning, K. W.: Trends in globally-averaged CO<sub>2</sub> determined from NOAA Global Monitoring Laboratory measurements, Version 2023-06, <https://doi.org/10.15138/9N0H-ZH07>, 2023.
- Large, W. G. and Yeager, S. G.: The Global Climatology of an Interannually Varying Air–Sea Flux Data Set, *Clim. Dynam.*, 33, 341–364, <https://doi.org/10.1007/s00382-008-0441-3>, 2009.
- Lauvset, S. K., Key, R. M., Olsen, A., van Heuven, S., Velo, A., Lin, X., Schirnick, C., Kozyr, A., Tanhua, T., Hoppema, M., Jutterström, S., Steinfeldt, R., Jeansson, E., Ishii, M., Perez, F. F., Suzuki, T., and Watelet, S.: A new global interior ocean mapped climatology: the 1° × 1° GLODAP version 2, *Earth Syst. Sci. Data*, 8, 325–340, <https://doi.org/10.5194/essd-8-325-2016>, 2016.
- Liu, K.-K. and Kaplan, I. R.: Denitrification rates and availability of organic matter in marine environments, *Earth Planet. Sc. Lett.*, 68, 88–100, 1984.
- Martin, J. H., Knauer, G. A., Karl, D. M., and Broenkow, W. W.: VERTEX: carbon cycling in the northeast Pacific, *Deep-Sea Res. Pt. I*, 34, 267–285, [https://doi.org/10.1016/0198-0149\(87\)90086-0](https://doi.org/10.1016/0198-0149(87)90086-0), 1987.
- Meinshausen, M., Smith, S. J., Calvin, K., Daniel, J. S., Kainuma, M. L., Lamarque, J.-F., Matsumoto, K., Montzka, S. A., Raper, S. C., Riahi, K., Thomson, A., Velders, G. J. M., and van Vuuren, D. P. P.: The RCP greenhouse gas concentrations and their extensions from 1765 to 2300, *Climatic Change*, 109, 213–241, 2011.
- Meinshausen, M., Vogel, E., Nauels, A., Lorbacher, K., Meinshausen, N., Etheridge, D. M., Fraser, P. J., Montzka, S. A., Rayner, P. J., Trudinger, C. M., Krummel, P. B., Beyerle, U., Canadell, J. G., Daniel, J. S., Enting, I. G., Law, R. M., Lunder, C. R., O’Doherty, S., Prinn, R. G., Reimann, S., Rubino, M., Velders, G. J. M., Vollmer, M. K., Wang, R. H. J., and Weiss, R.: Historical greenhouse gas concentrations for climate modelling (CMIP6), *Geosci. Model Dev.*, 10, 2057–2116, <https://doi.org/10.5194/gmd-10-2057-2017>, 2017.

- Middelburg, J. J., Soetaert, K., Herman, P. M. J., and Heip, C. H. R.: Denitrification in marine sediments: A model study, *Global Biogeochem. Cy.*, 10, 661–673, <https://doi.org/10.1029/96GB02562>, 1996.
- Middelburg, J. J., Soetaert, K., and Herman, P. M. J.: Empirical relationships for use in global diagenetic models, *Deep-Sea Res. Pt. I*, 44, 327–344, [https://doi.org/10.1016/S0967-0637\(96\)00101-X](https://doi.org/10.1016/S0967-0637(96)00101-X), 1997.
- Moreira Martinez, S., Roche, D. M., Munhoven, G., and Waelbroeck, C.: Coupling MEDUSA sediment model to iLOVE-CLIM (v1.1 $\beta$ ) Earth system model, in: 12th International Conference on Paleoceanography (ICP12), Utrecht (NL), 368 pp., <https://hdl.handle.net/2268/219749> (last access: 28 May 2021), 2016.
- Muller-Karger, F. E., Varela, R., Thunell, R., Luers sen, R., Hu, C., and Walsh, J. J.: The importance of continental margins in the global carbon cycle, *Geophys. Res. Lett.*, 32, L01602, <https://doi.org/10.1029/2004GL021346>, 2005.
- Munhoven, G.: Glacial–Interglacial Rain Ratio Changes: Implications for Atmospheric and Ocean–Sediment Interaction, *Deep-Sea Res. Pt. II*, 54, 722–746, <https://doi.org/10.1016/j.dsr2.2007.01.008>, 2007.
- Munhoven, G.: Model of Early Diagenesis in the Upper Sediment with Adaptable complexity – MEDUSA (v. 2): a time-dependent biogeochemical sediment module for Earth system models, process analysis and teaching, *Geosci. Model Dev.*, 14, 3603–3631, <https://doi.org/10.5194/gmd-14-3603-2021>, 2021.
- Nelson, D. M., Tréguer, P., Brzezinski, M. A., Leynaert, A., and Qu'éguiner, B.: Production and dissolution of biogenic silica in the ocean: Revised global estimates, comparison with regional data and relationship to biogenic sedimentation, *Global Biogeochem. Cy.*, 9, 359–372, <https://doi.org/10.1029/95GB01070>, 1995.
- Parameswaran, N., González, E., Burwicz-Galerie, E., Braack, M., and Wallmann, K.: NN-TOC v1: global prediction of total organic carbon in marine sediments using deep neural networks, *EGUsphere* [preprint], <https://doi.org/10.5194/egusphere-2024-1360>, 2024.
- Picard, A., Davis, R. S., Gläser, M., and Fujii, K.: Revised formula for the density of moist air (CIPM-2007), *Metrologia*, 45, 149–155, <https://doi.org/10.1088/0026-1394/45/2/004>, 2008.
- Sarmiento, J. L. and Gruber, N.: *Ocean Biogeochemical Dynamics*, Princeton University Press, <https://doi.org/10.2307/j.ctt3fgxqx>, 2006.
- Sarmiento, J. L., Dunne, J., Gnanadesikan, A., Key, R. M., Matsumoto, K., and Slater, R.: A new estimate of the CaCO<sub>3</sub> to organic carbon export ratio, *Global Biogeochem. Cy.*, 16, 1107, <https://doi.org/10.1029/2002GB001919>, 2002.
- Schartau, M., Engel, A., Schröter, J., Thoms, S., Völker, C., and Wolf-Gladrow, D.: Modelling carbon overconsumption and the formation of extracellular particulate organic carbon, *Biogeoosciences*, 4, 433–454, <https://doi.org/10.5194/bg-4-433-2007>, 2007.
- Scholz, P., Sidorenko, D., Gurses, O., Danilov, S., Koldunov, N., Wang, Q., Sein, D., Smolentseva, M., Rakowsky, N., and Jung, T.: Assessment of the Finite-volumE Sea ice–Ocean Model (FESOM2.0) – Part 1: Description of selected key model elements and comparison to its predecessor version, *Geosci. Model Dev.*, 12, 4875–4899, <https://doi.org/10.5194/gmd-12-4875-2019>, 2019.
- Scholz, P., Sidorenko, D., Danilov, S., Wang, Q., Koldunov, N., Sein, D., and Jung, T.: Assessment of the Finite-VolumE Sea ice–Ocean Model (FESOM2.0) – Part 2: Partial bottom cells, embedded sea ice and vertical mixing library CVMix, *Geosci. Model Dev.*, 15, 335–363, <https://doi.org/10.5194/gmd-15-335-2022>, 2022.
- Séférian, R., Berthet, S., Yool, A., Palmiéri, J., Bopp, L., Tagliabue, A., Kwiatkowski, L., Aumont, O., Christian, J., Dunne, J., Gehlen, M., Ilyina, T., John, J. G., Li, H., Long, M. C., Luo, J. Y., Nakano, H., Romanou, A., Schwinger, J., Stock, C., Santana-Falcón, Y., Takano, Y., Tjiputra, J., Tsujino, H., Watanabe, M., Wu, T., Wu, F., and Yamamoto, A.: Tracking Improvement in Simulated Marine Biogeochemistry Between CMIP5 and CMIP6, *Curr. Clim. Change Rep.*, 6, 95–119, <https://doi.org/10.1007/s40641-020-00160-0>, 2020.
- Seifert, M., Nissen, C., Rost, B., and Hauck, J.: Cascading effects augment the direct impact of CO<sub>2</sub> on phytoplankton growth in a biogeochemical model, *Elementa*, 10, 00104, <https://doi.org/10.1525/elementa.2021.00104>, 2022.
- Seiter, K., Hensen, C., Schröter, J., and Zabel, M.: Organic Carbon Content in Surface Sediments – Defining Regional Provinces, *Deep-Sea Res. Pt. I*, 51, 2001–2026, <https://doi.org/10.1016/j.dsr.2004.06.014>, 2004.
- Seiter, K., Hensen, C., and Zabel, M.: Benthic carbon mineralization on a global scale, *Global Biogeochem. Cy.*, 19, GB1010, <https://doi.org/10.1029/2004GB002225>, 2005.
- Shi, X., Cauquoin, A., Lohmann, G., Jonkers, L., Wang, Q., Yang, H., Sun, Y., and Werner, M.: Simulated stable water isotopes during the mid-Holocene and pre-industrial periods using AWI-ESM-2.1-wiso, *Geosci. Model Dev.*, 16, 5153–5178, <https://doi.org/10.5194/gmd-16-5153-2023>, 2023.
- Smith, S. V. and Hollibaugh, J. T.: Coastal Metabolism and the Oceanic Organic Carbon Balance, *Rev. Geophys.*, 31, 75–89, <https://doi.org/10.1029/92RG02584>, 1993.
- Snelgrove, P. V., Soetaert, K., Solan, M., Thrush, S., Wei, C.-L., Danovaro, R., Fulweiler, R. W., Kitazato, H., Ingole, B., Norkko, A., Parkes, R. J., and Volkenborn, N.: Global Carbon Cycling on a Heterogeneous Seafloor, *Trends Ecol. Evol.*, 33, 96–105, <https://doi.org/10.1016/j.tree.2017.11.004>, 2018.
- Soetaert, K., Herman, P. M. J., and Middelburg, J. J.: A model of early diagenetic processes from the shelf to abyssal depths, *Geochim. Cosmochim. Ac.*, 60, 1019–1040, [https://doi.org/10.1016/0016-7037\(96\)00013-0](https://doi.org/10.1016/0016-7037(96)00013-0), 1996.
- Steele, M., Morley, R., and Ermold, W.: PHC: A Global Ocean Hydrography with a High-Quality Arctic Ocean, *J. Climate*, 14, 2079–2087, [https://doi.org/10.1175/1520-0442\(2001\)014<2079:PAGOHW>2.0.CO;2](https://doi.org/10.1175/1520-0442(2001)014<2079:PAGOHW>2.0.CO;2), 2001.
- Stratmann, T., Wei, C.-L., Lin, Y.-S., and van Oevelen, D.: The SCOC database, a large, open, and global database with sediment community oxygen consumption rates, *Sci. Data*, 6, 242, <https://doi.org/10.1038/s41597-019-0259-3>, 2019.
- Thullner, M., Dale, A. W., and Regnier, P.: Global-scale quantification of mineralization pathways in marine sediments: A reaction-transport modeling approach, *Geochem. Geophys., Geosy.*, 10, Q10012, <https://doi.org/10.1029/2009GC002484>, 2009.
- Tréguer, P., Nelson, D. M., Bennekom, A. J. V., DeMaster, D. J., Leynaert, A., and Qu'éguiner, B.: The Silica Balance

- in the World Ocean: A Reestimate, *Science*, 268, 375–379, <https://doi.org/10.1126/science.268.5209.375>, 1995.
- Tréguer, P. J. and De La Rocha, C. L.: The World Ocean Silica Cycle, *Annu. Rev. Mar. Sci.*, 5, 477–501, <https://doi.org/10.1146/annurev-marine-121211-172346>, 2013.
- Tréguer, P. J., Sutton, J. N., Brzezinski, M., Charette, M. A., Devries, T., Dutkiewicz, S., Ehlert, C., Hawkings, J., Leynaert, A., Liu, S. M., Llopis Monferrer, N., López-Acosta, M., Maldonado, M., Rahman, S., Ran, L., and Rouxel, O.: Reviews and syntheses: The biogeochemical cycle of silicon in the modern ocean, *Biogeosciences*, 18, 1269–1289, <https://doi.org/10.5194/bg-18-1269-2021>, 2021.
- Trenberth, K. E. and Smith, L.: The Mass of the Atmosphere: A Constraint on Global Analyses, *J. Climate*, 18, 864–875, <https://doi.org/10.1175/JCLI-3299.1>, 2005.
- Volk, T. and Hoffert, M. I.: Ocean Carbon Pumps: Analysis of Relative Strengths and Efficiencies in Ocean-Driven Atmospheric CO<sub>2</sub> Changes, in: *The Carbon Cycle and Atmospheric CO<sub>2</sub>: Natural Variations Archean to Present*, edited by: Sundquist, E. T. and Broecker, W. S., vol. 32 of *Geophysical Monograph Series*, American Geophysical Union (AGU), Washington (DC), 99–110, <https://doi.org/10.1029/GM032p0099>, 1985.
- Wanninkhof, R.: Relationship between wind speed and gas exchange over the ocean revisited, *Limnol. Oceanogr.*, 12, 351–362, <https://doi.org/10.4319/lom.2014.12.351>, 2014.
- Ye, Y.: Ocean biogeochemistry model FESOM2.1-REcoM3 coupled with a sediment model MEDUSA2, Zenodo [code], <https://doi.org/10.5281/zenodo.8315240>, 2023.
- Ye, Y.: FESOM2.1-REcoM3-MEDUSA2: an ocean-sea ice-biogeochemistry model coupled to a sediment model, Zenodo [data set], <https://doi.org/10.5281/zenodo.14887815>, 2025.
- Zeebe, R. E. and Wolf-Gladrow, D. A.: CO<sub>2</sub> in Seawater: Equilibrium, Kinetics, Isotopes, vol. 65 of *Elsevier Oceanography Book Series*, Elsevier Science Publishing, Amsterdam, The Netherlands, ISBN 978-0-444-50946-8, 2001.





*Supplement of*

## **FESOM2.1-REcoM3-MEDUSA2: an ocean–sea ice–biogeochemistry model coupled to a sediment model**

**Ying Ye et al.**

*Correspondence to:* Ying Ye ([ying.ye@awi.de](mailto:ying.ye@awi.de))

The copyright of individual parts of the supplement might differ from the article licence.

# MEDUSA Setup and Selected Configuration Options

## S1 Formulation

### S1.1 Early diagenetic reaction network and chemical composition

The reaction network set up in this version of MEDUSA includes the following processes:

- Calcite dissolution;
- Opal dissolution;
- Organic Matter (OM) degradation: three different pathways are considered
  - oxic respiration
  - nitrate reduction
  - sulfate reduction

Mn(IV) and Fe(III) reduction pathways are disregarded here as they play, globally speaking, only negligible roles as TEAs (terminal electron acceptors) in comparison to the three pathways considered with  $O_2$ ,  $NO_3^-$  and  $SO_4^{2-}$  as TEAs, resp. (Thullner et al., 2009).

The adopted model configuration includes  $CO_2$ ,  $HCO_3^-$ ,  $CO_3^{2-}$ ,  $O_2$ ,  $NO_3^-$  and  $NH_4^+$  as solutes, and two classes of organic matter (a fast and a slowly metabolizable one), clay and calcite as solids. For simplicity, the  $\Sigma NH_3$  and  $\Sigma H_2S$  systems are reduced to  $NH_4^+$  and  $HS^-$ , resp.

### S1.2 Boundary conditions

Temperature, pressure and salinity for each sediment column are those of the bottom ocean cell that it is in contact with and similarly for the solutes' concentrations at the sediment–water–interface (SWI). The boundary conditions for  $NH_4^+$ ,  $HS^-$  and  $SO_4^{2-}$ , which are not among the tracers considered in REcoM3p, the REcoM3 variant used here, are set as follows: the concentrations of  $NH_4^+$  and  $HS^-$  at the SWI is set to 0 (Jourabchi et al., 2008; Thullner et al., 2009) and that of  $SO_4^{2-}$  is derived from the sulfate–salinity relationship, i.e.  $[SO_4^{2-}]_{SWI} / [mol (kg-SW)^{-1}] = (0.14/96.062) \times (S/1.80655)$  (Dickson et al., 2007, chap. 6, p. 10), where  $S$  is the salinity at the SWI.

For solids, a flux-continuity condition is adopted at the SWI: solid material deposited at the sea-floor gets transferred to the sediment across the SWI.

The organic matter REcoM3p has a C : N(: P) composition that varies in space and time. C : N : P compositions of organic matter classes in MEDUSA may, must, however, remain constant in time; they may only be spatially variable. Organic matter reaching the sea-floor is therefore handled as if it was a mixture of two end-member classes, each one with a fixed C : N : P ratio: one with C : N = 106 : 21 : 1.3125 (fast metabolizable), and one with C : N : P = 200 : 11 : 0.6875 (slowly metabolizable). Since REcoM3p does not consider P, the N : P ratio of the two end-member classes in MEDUSA is assumed to be at the Redfield ratio of 16:1.

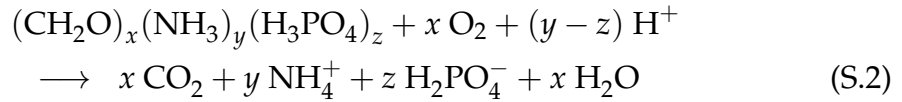
### S1.3 Model reactions

The equations used to represent the chemical reactions that describe the processes considered are as follows:

$R^1$  — CaCO<sub>3</sub> dissolution:

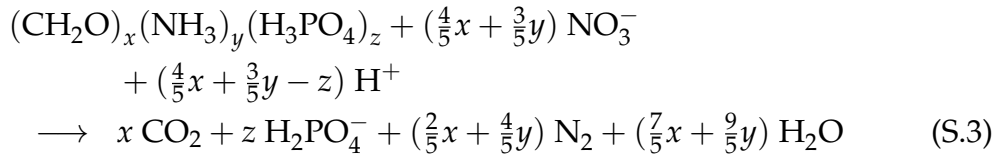


$R^2$  &  $R^3$  – oxidation of ‘fast’ and ‘slow’ OM classes, resp., by oxic respiration:

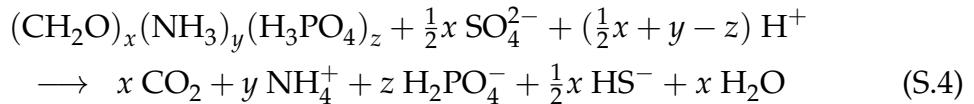


where  $x = 106$ ,  $y = 21$  and  $z = 1.3125$  for the ‘fast,’ and  $x = 200$ ,  $y = 11$  and  $z = 0.6875$  for the ‘slow’ OM class

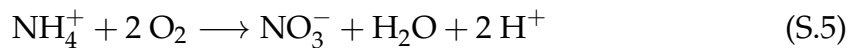
$R^4$  &  $R^5$  – oxidation of ‘fast’ and ‘slow’ OM classes, resp., by nitrate reduction and full denitrification:



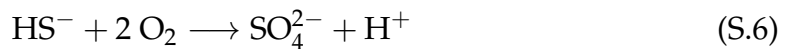
$R^6$  &  $R^7$  – oxidation of ‘fast’ and ‘slow’ OM classes, resp., by sulfate reduction:



$R^8$  – ammonium re-oxidation by O<sub>2</sub>:



$R^9$  – sulfide re-oxidation by O<sub>2</sub>:



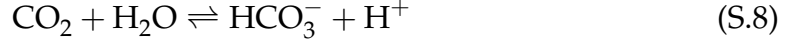
$R^{10}$  – opal dissolution:



## S1.4 Equilibria

As a consequence of the simplifications adopted for the ammonium and hydrogen sulfide (hydrosulfuric acid) systems, only the carbonate system equilibria need to be considered:

$E^1$  (first dissociation of carbonic acid):



$E^2$  (second dissociation of carbonic acid):



## S2 Unified Formulation

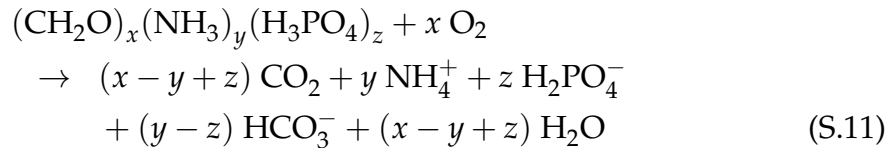
The equations from the previous section are modified in order to discard the  $\text{H}^+$  ion, by introduction of the  $\text{CO}_2\text{--HCO}_3^-$  equilibrium  $\text{CO}_2 + \text{H}_2\text{O} \rightleftharpoons \text{HCO}_3^- + \text{H}^+$ . Accordingly, if one side of chemical reaction includes a term  $n \text{H}^+$ , that term is substituted with  $n \text{CO}_2 + n \text{H}_2\text{O}$ , and a term  $n \text{HCO}_3^-$  is added to the other side. Finally, the two equilibria  $E^1$  and  $E^2$  are furthermore lumped into one ( $E^{1+2}$ ).

This same procedure was also adopted by Wang and Van Cappellen (1996) and Thullner et al. (2009).

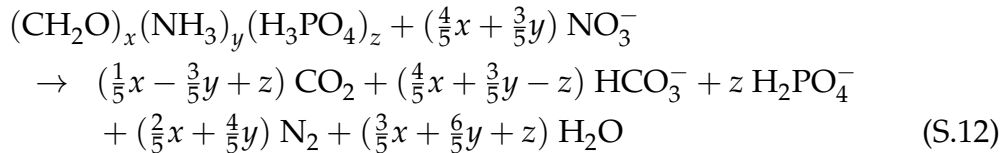
$R^1$  ( $\text{CaCO}_3$  dissolution):



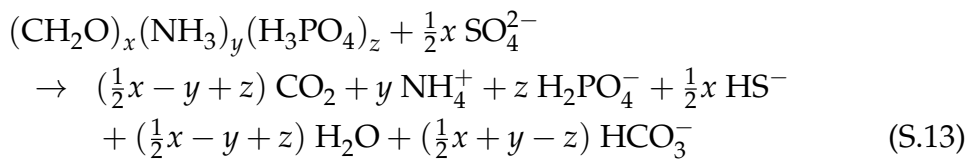
$R^2$  &  $R^3$  (oxic respiration):



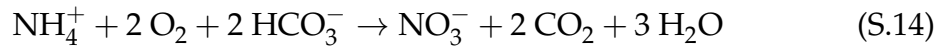
$R^4$  &  $R^5$  (nitrate reduction):



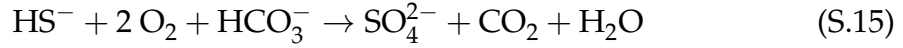
$R^6$  &  $R^7$  (sulfate reduction):



$R^8$  (ammonium re-oxidation):



$R^9$  (sulfide re-oxidation):



$R^{10}$  (opal dissolution):



## S2.1 Equilibrium

$E^{1+2}$  (carbonate system equilibrium):



## S3 Kinetic Rate Laws and Equilibrium Relationship

Reaction rates are written here as  $\hat{R}$  values, i.e., per unit volume of total sediment (solids + porewater): for solids' degradation/dissolution rates, units are each time kg solid  $(\text{m}^3 \text{ total sediment})^{-1} \text{ yr}^{-1}$ ; for reactions between solutes only, the rates are expressed in mol solute  $(\text{m}^3 \text{ total sediment})^{-1} \text{ yr}^{-1}$ .

### S3.1 Calcite dissolution

The classical formulation in  $(1 - \Omega)^{4.5}$  (Keir, 1980; Archer, 1991) was adopted:

$$\hat{R}_1 = k_1(1 - \varphi) \cdot [\text{Calc}] \cdot ((1 - [\text{CO}_3^{2-}]/C_{\text{cs}})^{\oplus})^{n_1}$$

where

- $k_1 = 1 \text{ d}^{-1} = 365.25 \text{ yr}^{-1}$  (Archer, 1991);
- $n_1 = 4.5$  (Keir, 1980; Archer, 1991);
- $(\dots)^{\oplus}$  denotes the positive part of  $(\dots)$ ;
- $C_{\text{cs}}$  is the  $\text{CO}_3^{2-}$  concentration at saturation with respect to calcite in seawater.

### S3.2 OM oxidation by oxic respiration

The rate of oxic respiration (eq. S.11) is proportional to the concentration of organic matter (OM) and to a (hyperbolic) Monod factor in the porewater concentration of  $O_2$ :

$$\hat{R}_{2,3} = k_{f,s}(1 - \varphi) \cdot [OM_{f,s}] \cdot \frac{[O_2]}{C_{\text{hox}} + [O_2]},$$

where

- $k_f = 3.2 \times 10^{-1} \text{ yr}^{-1}$  (for  $\hat{R}_2$ );
- $k_s = 3.2 \times 10^{-3} \text{ yr}^{-1}$  (for  $\hat{R}_3$ );
- $C_{\text{hox}} = 3 \mu\text{mol L}^{-1}$  (Soetaert et al., 1996) is the half-saturation concentration of  $O_2$  for the oxic remineralisation of organic matter; the same value is used for both fast and slow OM classes.

The values for  $k_f$  and  $k_s$  were derived by considering typical deep-sea values of  $10^{-9} \text{ s}^{-1} \simeq 3.2 \times 10^{-2} \text{ yr}^{-1}$  (e.g., Emerson, 1985; Archer, 1991). The finally adopted values were then derived by adopting a two-order of magnitude difference between the slow and fast metabolizable classes (Soetaert et al., 1996), which led us to adopt a one order of magnitude higher value than the typical one for the fast metabolizable class (i.e.,  $k_f = 3.2 \times 10^{-1} \text{ yr}^{-1}$ ) and a one order of magnitude lower value for the slowly metabolizable class (i.e.,  $k_s = 3.2 \times 10^{-3} \text{ yr}^{-1}$ ).

### S3.3 OM oxidation by nitrate reduction, with full denitrification

The rate of OM degradation by nitrate reduction, and full denitrification ( $R^4$  and  $R^5$ , Eq. S.12), is again proportional to the concentration of OM. It is furthermore proportional to a Monod factor in the porewater concentration of  $NO_3^-$ , and to a hyperbolic inhibition factor in the porewater concentration of  $O_2$ :

$$\hat{R}_{4,5} = k_{f,s}(1 - \varphi) \cdot [OM_{f,s}] \cdot \frac{[NO_3^-]}{C_{\text{hnr}} + [NO_3^-]} \cdot \frac{C_{\text{ino}}}{C_{\text{ino}} + [O_2]},$$

where

- $k_f$  and  $k_s$  are the same as in  $\hat{R}_2$  and  $\hat{R}_3$  above;
- $C_{\text{hnr}} = 30 \mu\text{mol L}^{-1}$  (Soetaert et al., 1996) is the half-saturation concentration of  $NO_3^-$  for organic matter degradation by nitrate reduction and denitrification;
- $C_{\text{ino}} = 10 \mu\text{mol L}^{-1}$  (Soetaert et al., 1996) is the characteristic inhibition concentration of  $O_2$  for the oxidation of organic matter by nitrate reduction.

The same  $C_{\text{hnr}}$  and  $C_{\text{ino}}$  are used for slow and fast metabolizable OM.

### S3.4 OM oxidation by sulfate reduction

The rate of OM degradation by sulfate reduction ( $R^6$  and  $R^7$ , Eq. S.13) is again proportional to the concentration of OM. It is furthermore proportional to a Monod factor in the porewater concentration of  $\text{SO}_4^{2-}$ , and to two hyperbolic inhibition factors in the porewater concentrations of  $\text{NO}_3^-$  and  $\text{O}_2$ , resp.:

$$\hat{R}_{6,7} = k_{f,s}(1 - \varphi) \cdot [\text{OM}_{f,s}] \cdot \frac{[\text{SO}_4^{2-}]}{C_{\text{hsr}} + [\text{SO}_4^{2-}]} \cdot \frac{C_{\text{isn}}}{C_{\text{isn}} + [\text{NO}_3^-]} \cdot \frac{C_{\text{iso}}}{C_{\text{iso}} + [\text{O}_2]}$$

with

- $k_f$  and  $k_s$  are the same as in  $\hat{R}_2$  and  $\hat{R}_3$  above;
- $C_{\text{hsr}} = 0.5 \text{ mmol L}^{-1}$  is the half-saturation concentration of  $\text{SO}_4^{2-}$  for organic matter degradation by sulfate reduction, derived from the value of  $1 \text{ mmol L}^{-1}$  that Jourabchi et al. (2008) adopted in their ramp-law;
- $C_{\text{isn}} = 5 \mu\text{mol L}^{-1}$  (Soetaert et al., 1996) is the characteristic inhibition concentration of  $\text{NO}_3^-$  for the oxidation of organic matter by sulfate reduction;
- $C_{\text{iso}} = 10 \mu\text{mol L}^{-1}$  (Soetaert et al., 1996) is the characteristic inhibition concentration of  $\text{O}_2$  for the oxidation of organic matter by sulfate reduction.

The same  $C_{\text{hsr}}$ ,  $C_{\text{iso}}$  and  $C_{\text{isn}}$  are used for slow and fast metabolizable OM.

### S3.5 Ammonium re-oxidation by $\text{O}_2$ (nitrification)

The rate of oxidation of  $\text{NH}_4^+$  by  $\text{O}_2$  (eq. S.14) is first order in both  $[\text{NH}_4^+]$  and  $[\text{O}_2]$ .

$$\hat{R}_8 = k_8 \varphi \cdot [\text{NH}_4^+] \cdot [\text{O}_2]$$

The rate constant  $k_8$  is set to  $10^4 (\text{mol/m}^3)^{-1} \text{yr}^{-1}$  (Jourabchi et al., 2008).

### S3.6 Sulfide re-oxidation by $\text{O}_2$

Oxidation of  $\text{HS}^-$  by  $\text{O}_2$  (eq. S.15): first order in both  $[\text{HS}^-]$  and  $[\text{O}_2]$

$$\hat{R}_9 = k_9 \varphi \cdot [\text{HS}^-] \cdot [\text{O}_2]$$

Selecting a value for the rate constant  $k_9$  proved tricky. Previously published models used widely different values\*:

- Van Cappellen and Wang (1995) set it to  $3 \times 10^8 \text{ M}^{-1} \text{yr}^{-1}$  in the deep sea and to  $6 \times 10^8 \text{ M}^{-1} \text{yr}^{-1}$  on the shelves, with reference to Morse et al. (1987);

---

\*In the following, the quoted figures are expressed in the units in which they were reported in the respective references, and 'M' is understood to stand for  $\text{mol L}^{-1}$ .

- Van Cappellen and Wang (1996) and Wang and Van Cappellen (1996) set it to  $1.6 \times 10^5 \text{ M}^{-1} \text{ yr}^{-1}$ , with reference to Millero et al. (1987);
- Jourabchi et al. (2008) set it to  $3 \times 10^8 \text{ M}^{-1} \text{ yr}^{-1}$ , with reference to Van Cappellen and Wang (1995);
- Thullner et al. (2009) set it to  $3 \times 10^8 \text{ M}^{-1} \text{ yr}^{-1}$ , with reference to Van Cappellen and Wang (1995);
- Arndt et al. (2011) use a different rate law expression:

$$R_{A11} = k_{T_S, O_2} \cdot \frac{O_2}{K_{T_{O_2}, \text{redox}} + O_2} \cdot T_S,$$

with  $k_{T_S, O_2} = 6 \text{ yr}^{-1}$  (calibrated) and  $K_{T_{O_2}, \text{redox}} = 20 \text{ mmol m}^{-3}$ . The coefficients in the two expressions can only be compared for  $O_2 \ll K_{T_{O_2}, \text{redox}}$ , in which case  $k_9 \simeq k_{T_S, O_2} / K_{T_{O_2}, \text{redox}} = 6/20 = 0.3 \text{ (mmol m}^{-3})^{-1} \text{ yr}^{-1} = 3 \times 10^5 \text{ M}^{-1} \text{ yr}^{-1}$ .

This three orders of magnitude differences between the adopted values seem difficult to reconcile a priori. However, it appears that the rate of sulfide oxidation strongly depends on whether it takes place inorganically or is biologically mediated. In this latter case, it may indeed proceed orders of magnitude faster than in abiotic cases (the presence of  $\text{Fe}^{2+}$  or  $\text{Mn}^{2+}$  also appears to promote the reaction, albeit to a lesser extent).

We therefore chose to use  $k_9 = 5 \times 10^5 \text{ (mol m}^{-3})^{-1} \text{ yr}^{-1}$ , a value intermediate between the deep-sea and shelf values of Van Cappellen and Wang (1995), slightly biased towards the shelf end-member, as the reaction is important mainly in shallower waters in our model.

### S3.7 Opal dissolution

The opal dissolution rate expression in  $(C_{\text{sat}} - C)$  (Boudreau, 1990) is considered. Accordingly, the dissolution rate is taken to be proportional to the opal content itself, and to the difference from the saturation concentration of  $\text{H}_4\text{SiO}_4$  with respect to opal:

$$\hat{R}_{10} = k_{10}(1 - \varphi) \cdot [\text{Opal}] \cdot (C_{\text{osp}} - [\text{H}_4\text{SiO}_4])^{\oplus}$$

where

- $k_{10} = 0.03 \text{ (mol/m}^3)^{-1} \text{ yr}^{-1}$ ;
- $C_{\text{osp}}$  is the asymptotic (“saturation”) concentration for opal dissolution, set here to  $1000 \mu\text{mol kg-SW}^{-1}$  (Archer et al., 1993, following Hurd, 1973);
- and  $(\dots)^{\oplus}$  denotes again the positive part of  $(\dots)$ .



### S3.8 Carbonate equilibrium

The equilibrium constant for the chemical equilibrium (S.17) is derived from the local sediment-top boundary conditions for  $[\text{CO}_2]$ ,  $[\text{HCO}_3^-]$ , and  $[\text{CO}_3^{2-}]$ , (standard procedure in MEDUSA). As a consequence, the equilibrium constant is consistent with the carbonate speciation in the host model (REcoM3p).

## S4 Spatial Extent and Discretization Grid

The model sediment columns extend down to 50 cm below the sediment–water interface. The top-most 10 cm are mixed by bioturbation. The mixed-layer part is covered with a node-to-node grid of 21 points; the 40 cm below are also covered by a node-to-node grid with an additional 50 points (total of 71 points). Both sub-grids follow a 50%–50% quadratic–linear distribution (please refer to the *Technical Reference* in the Supplement to Munhoven (2021) for details about how to set grid properties in MEDUSA v.2).

## S5 Milieu Characteristics

A static global exponentially decreasing porosity profile is used for all sediment columns:

$$\varphi(z) = \varphi_0 + (\varphi_0 - \varphi_\infty) \exp(-z/\zeta)$$

where

- $z$  is the depth in the sediment below the SWI, located at  $z = 0$ , and increasing downwards;
- $\varphi_0 = 0.9$  is the porosity at the SWI;
- $\varphi_\infty = 0.7$  is the porosity at great depth;
- $\zeta = 4$  cm is the spatial scale of variation (Soetaert et al., 1996)

Tortuosity,  $\vartheta^2$ , is parametrised as a function of porosity using the modified Weissberg relationship from Boudreau (1997, p. 131):

$$\vartheta^2 = 1 - 2.02 \ln \varphi.$$

## S6 Transport Parameters

### S6.1 Advection

As all the solids are considered with their physical specific volumes, advection is treated in the usual way (i.e., the advection rate profile is at each time step derived

iteratively from the integrated reaction rate profile). Please refer to Munhoven (2021) for details about how this is done.

## S6.1 Bioturbation

Bioturbation is represented as a diffusive process (biodiffusion). The bioturbation coefficient  $D_b$  is uniformly set to  $0.150 \text{ cm}^2/\text{yr}$ , a typical deep-sea value (Emerson, 1985).

## S7 Closing the Global Material Balances

### S7.1 Loopback fluxes

In order to conserve the total amounts of carbon and other nutrients, as well as alkalinity in the combined ocean–sediment system, solids that leave the model sediment through its lower boundary (at 50 cm depth below the SWI) are formally remineralized and the resulting amounts of carbon, nutrients and alkalinity returned to the surface, mimicking riverine input to the ocean.

### S7.2 Compensating for nutrient sinks and alkalinity sources during anoxic OM degradation

The sediment takes up  $\text{SO}_4^{2-}$  for the oxidation of OM by sulfate reduction. Part of the  $\text{HS}^-$  produced during OM oxidation by sulfate reduction is re-oxidized to  $\text{SO}_4^{2-}$  in the oxygenated part of the sediment, but part is not and diffuses back to the overlying bottom seawater. Please notice that, although the boundary conditions at the SWI set the  $\text{HS}^-$  concentration to 0, this does not imply that the diffusive return flux to the ocean is 0 as well. This latter indeed depends on the sediment–side  $\text{HS}^-$  concentration gradient, which is not necessarily 0. Although imbalances in the sulfate content of the ocean would be without consequences, the conversion of  $\text{SO}_4^{2-}$  to  $\text{HS}^-$  has a non-negligible effect on the alkalinity balance of the ocean, as  $\text{HS}^-$  carries alkalinity, while  $\text{SO}_4^{2-}$  does not. Similarly, the alkalinity balance of the ocean will be disturbed by nitrogen that returns to the ocean as  $\text{NH}_4^+$  instead of  $\text{NO}_3^-$ .

Accordingly, reactions (S.14) and (S.15) are also considered to implicitly take place at (the ocean-side of) the SWI, neutralising the diffusive return fluxes of  $\text{NH}_4^+$  and  $\text{HS}^-$  to the ocean, and the impact of these reactions on the alkalinity in the bottom ocean water accounted for:

- for ammonium re-oxidation (reaction S.5 or S.14), we have  $\Delta\text{Alk}_T = -\Delta\text{TNO}_3 + \Delta\text{TNH}_3 = 2\Delta\text{TNH}_3$ , since  $\Delta\text{TNO}_3 = -\Delta\text{TNH}_3$  in those equations;
- for sulfide re-oxidation (reaction S.6 or S.15), we have  $\Delta\text{Alk}_T = -2\Delta\text{TSO}_4 = 2\Delta\text{HS}^-$ , since  $\Delta\text{TSO}_4 = -\Delta\text{HS}^-$  in those equations.

Here we have called up the explicit conservative expression of alkalinity (Wolf-Gladrow et al., 2007) to link  $\Delta\text{Alk}_T$  to the other variations. Let us then denote the diffusive return fluxes of  $\text{NH}_4^+$  and  $\text{HS}^-$  to the ocean provided by MEDUSA by  $J_{\text{NH}_4^+}$  and  $J_{\text{HS}^-}$ , supposed to be positive as they represent sources for the ocean. Accordingly,  $\Delta\text{TNH}_3 = -J_{\text{NH}_4^+} < 0$  and  $\Delta\text{HS}^- = -J_{\text{HS}^-} < 0$ , and we find that the above reactions provide an alkalinity *sink* equal to  $2 \times (J_{\text{NH}_4^+} + J_{\text{HS}^-})$  in the bottom ocean water.

## References

- Archer, D., Lyle, M., Rodgers, K., and Froelich, P.: What Controls Opal Preservation in Tropical Deep-Sea Sediments?, *Paleoceanography*, 8, 7–21, <https://doi.org/10.1029/92PA02803>, 1993.
- Archer, D. E.: Modeling the Calcite Lysocline, *J. Geophys. Res.*, 96, 17 037–17 050, <https://doi.org/10.1029/91JC01812>, 1991.
- Arndt, S., Regnier, P., Godd eris, Y., and Donnadieu, Y.: GEOCLIM *reloaded* (v 1.0): a new coupled earth system model for past climate change, *Geosci. Model Dev.*, 4, 451–481, <https://doi.org/10.5194/gmd-4-451-2011>, 2011.
- Boudreau, B. P.: Asymptotic forms and solutions of the model for silica-opal diagenesis in bioturbated sediments, *J. Geophys. Res.*, 95, 7367–7379, <https://doi.org/10.1029/JC095iC05p07367>, 1990.
- Boudreau, B. P.: *Diagenetic Models and Their Implementation*, Springer-Verlag, Berlin (DE), 1997.
- Dickson, A. G., Sabine, C. L., and Christian, J. R., eds.: Guide to Best Practices for Ocean CO<sub>2</sub> Measurements, vol. 3 of *PICES Special Publication*, Carbon Dioxide Information and Analysis Center, Oak Ridge (TN), URL [https://www.ncei.noaa.gov/access/ocean-carbon-acidification-data-system/oceans/Handbook\\_2007.html](https://www.ncei.noaa.gov/access/ocean-carbon-acidification-data-system/oceans/Handbook_2007.html), 2007.
- Emerson, S.: Organic carbon preservation in marine sediments, in: *The Carbon Cycle and Atmospheric CO<sub>2</sub>: Natural Variations Archean to Present*, edited by Sundquist, E. T. and Broecker, W. S., vol. 32 of *Geophys. Monogr. Ser.*, pp. 78–87, AGU, Washington (DC), <https://doi.org/10.1029/GM032p0078>, 1985.
- Hurd, D. C.: Interactions of biogenic opal, sediment and seawater in the Central Equatorial Pacific, *Geochim. Cosmochim. Acta*, 37, 2257–2282, [https://doi.org/10.1016/0016-7037\(73\)90103-8](https://doi.org/10.1016/0016-7037(73)90103-8), 1973.
- Jourabchi, P., Meile, C., Pasion, L. R., and Van Cappellen, P.: Quantitative interpretation of pore water O<sub>2</sub> and pH distributions in deep-sea sediments,

- Geochim. Cosmochim. Acta, 72, 1350–1364, <https://doi.org/10.1016/j.gca.2007.12.012>, 2008.
- Keir, R. S.: The dissolution kinetics of biogenic calcium carbonates in seawater, *Geochim. Cosmochim. Acta*, 44, 241–252, [https://doi.org/10.1016/0016-7037\(80\)90135-0](https://doi.org/10.1016/0016-7037(80)90135-0), 1980.
- Millero, F. J., Hubinger, S., Fernandez, M., and Garnett, S.: Oxidation of H<sub>2</sub>S in seawater as a function of temperature, pH, and ionic strength, *Environ. Sci. Technol.*, 21, 439–443, <https://doi.org/10.1021/es00159a003>, 1987.
- Morse, J., Millero, F., Cornwell, J., and Rickard, D.: The chemistry of the hydrogen sulfide and iron sulfide systems in natural waters, *Earth Sci. Rev.*, 24, 1–42, [https://doi.org/10.1016/0012-8252\(87\)90046-8](https://doi.org/10.1016/0012-8252(87)90046-8), 1987.
- Munhoven, G.: Model of Early Diagenesis in the Upper Sediment with Adaptable complexity – MEDUSA (v. 2): a time-dependent biogeochemical sediment module for Earth system models, process analysis and teaching, *Geosci. Model Dev.*, 14, 3603–3631, <https://doi.org/10.5194/gmd-14-3603-2021>, 2021.
- Soetaert, K., Herman, P. M. J., and Middelburg, J. J.: A model of early diagenetic processes from the shelf to abyssal depths, *Geochim. Cosmochim. Acta*, 60, 1019–1040, [https://doi.org/10.1016/0016-7037\(96\)00013-0](https://doi.org/10.1016/0016-7037(96)00013-0), 1996.
- Thullner, M., Dale, A. W., and Regnier, P.: Global-scale quantification of mineralization pathways in marine sediments: A reaction-transport modeling approach, *Geochem., Geophys., Geosyst.*, 10, Q10012, <https://doi.org/10.1029/2009GC002484>, 2009.
- Van Cappellen, P. and Wang, Y.: Metal Cycling in Surface Sediments: Modeling the Interplay of Transport and Reaction, in: *Metal Contaminated Aquatic Sediments*, edited by Allen, H. E., chap. 2, pp. 21–64, Ann Arbor Press, <https://doi.org/10.1201/9780203747643-2>, 1995.
- Van Cappellen, P. and Wang, Y.: Cycling of Iron and Manganese in Surface Sediments: A General Theory for the Coupled Transport and Reaction of Carbon, Oxygen, Nitrogen, Sulfur, Iron, and Manganese, *Am. J. Sci.*, 296, 197–243, <https://doi.org/10.2475/ajs.296.3.197>, 1996.
- Wang, Y. and Van Cappellen, P.: A multicomponent reactive transport model of early diagenesis: Application to redox cycling in coastal marine sediments, *Geochim. Cosmochim. Acta*, 60, 2993–3014, [https://doi.org/10.1016/0016-7037\(96\)00140-8](https://doi.org/10.1016/0016-7037(96)00140-8), 1996.
- Wolf-Gladrow, D. A., Zeebe, R. E., Klaas, C., Körtzinger, A., and Dickson, A. G.: Total alkalinity: The explicit conservative expression and its application to biogeochemical processes, *Mar. Chem.*, 106, 287–300, <https://doi.org/10.1016/j.marchem.2007.01.006>, 2007.